Tesis Doctoral

Experimental study of high-speed phenomena involving bubbles and free surfaces: bubble growth in microgravity and fast lifting of a plate from a water surface

Autora

Patricia Vega Martínez

Tesis depositada en cumplimiento parcial de los requisitos para el grado de Doctor en Mecánica de Fluidos.

UNIVERSIDAD CARLOS III DE MADRID

Director

Javier Rodríguez Rodríguez

Leganés, noviembre 2019

Esta tesis se distribuye bajo licencia "Creative Commons **Reconocimiento - No Comercial - Sin Obra Derivada**"

A la casualidad.
A mamá, papá y a mi bro, Sergio.

"Uno nunca se da cuenta de lo que se ha hecho, sólo puede ver lo que queda por hacer."

– Marie Curie (1867-1934)

"Cuando se habla sobre el aprendizaje y las ciencias, la gente no piensa en las mujeres."

– Wang Zhenyi (1768-1797)

Published and submitted content

The material from the following sources included in this thesis are not singled out with typographic:

- Vega-Martínez, Patricia, Rodríguez-Rodríguez, Javier, van der Meer, Devaraj & Sperl, Matthias 2017 Drop tower setup to study the diffusion-driven growth of a foam ball in supersaturated liquids in microgravity conditions. *Microgravity science and technology* **29** (4), 297–304.
  This publication is totally included in **part I** of this PhD thesis.

- Vega-Martínez, Patricia, Rodríguez-Rodríguez, Javier, Khabakhpasheva, TI & Korobkin, AA 2019*a* Hydroelastic effects during the fast lifting of a disc from a water surface. *Journal of Fluid Mechanics* **869**, 726–751.
  This publication is totally included in **part II** of this PhD thesis.

- Vega-Martínez, P, Rodríguez-Rodríguez, J, Khabakhpasheva, TI & Korobkin, AA 2019*b* Hydroelastic effects during the fast lifting of a disc from a water surface–corrigendum. *Journal of Fluid Mechanics* **878**, 932–933.
  This publication is totally included in **part II** of this PhD thesis.

- Vega-Martínez, Patricia, Rodríguez-Rodríguez, Javier & van der Meer, Devaraj 2019 (In preparation) Growth of a bubble cloud co_2-saturated water in microgravity. *Soft Matter.*
  This future publication is totally included in **part I** of this PhD thesis.

Other research merits

During this PhD thesis, the following paper have been published but they are not included in the document.

- Vega-Martínez, Patricia, Enríquez, Oscar R & Rodríguez-Rodríguez, Javier 2017 Some topics on the physics of bubble dynamics in beer. *Beverages* **3** (3), 38
- Igualada-Villodre, Elena, Medina-Palomo, Ana, Vega-Martínez, Patricia & Rodríguez-Rodríguez, Javier 2018 Transient effects in the translation of bubbles insonated with acoustic pulses of finite duration. *Journal of Fluid Mechanics* **836**, 649–693

Abstract

This thesis addresses two different problems with a *common* link: both are experimental studies where the effect of gravity does not play an important role. While the first one is in microgravity conditions, the other one shows an acceleration much greater than gravity. As a consequence, this dissertation is divided into two parts: growing bubbles in gas-supersaturated liquid in microgravity and fast lifting of a plate from a water surface.

In the first part, the diffusion-driven growth of a dense bubble cloud is studied in gas-supersaturated liquid in microgravity conditions. Understanding the diffusive-driven dynamics is relevant in several modern technologies such as space manufacturing or chemistry processes as well as in the formation of the small planetary bodies if we move to the geological field. On Earth's conditions, it is not possible to observe this purely diffusion-driven growth for more than 100 ms since the gravity induces buoyancy effects that affects in these dynamics. Thus, we carried out experiments in which a bubble cloud grows in a CO_2-supersaturated water in microgravity using of the drop tower of the German Center of Applied Space Technology and Microgravity (ZARM). In the experiments, the evolution of the bubble cloud can be observed for more than 3 s as well as their interactions and competition to access the CO_2 available in the bulk liquid outside the cloud. Firstly, we show the details of the experimental setup that we use to perform these experiments and some preliminary results related to the individual growth of large bubbles and the time evolution of the gas volume of the cloud. Then, we report the existence of different regimes where the bubble cloud presents different growth rates in our experiments. Finally, we suggest a model that describes these regimes and their corresponding growth rate, qualitatively.

In the second part, we address an experimental research regarding the fast lifting of a circular disc from a water surface. For naval and ocean engineering it is essential to model the force that a structure must withstand when it impacts or exits the water. Since full-scale numerical simulations are usually impractical for this purpose, several analytical or semi-analytical approaches have been developed over the years. Due to the complexity of the free surface flows involving both numerical and analytical computations must be validated against experiments. With this idea in mind, here we report the results of the experimental measurements of the hydrodynamic force acting on a plate that is lifted from the water surface and starts to move upwards suddenly at an acceleration much larger than gravity, $a \gg g$. Furthermore, we include the hydro-elastic effect that we observed in the experiments in the solution of the asymmetric of the water exit problem. Our work focuses on the early stages of the disc motion when the suction and inertial forces are the most relevant. Thus, the experimental set-up is described firstly, then we compare the experimental results against the linearised theory of the water exit proposed by Korobkin (2013). Finally, as a consequence of the experimental observations of the hydroelastic interaction between the disc and the liquid, the problem of the water exit is reformulated and solved taking into account this effect.

Resumen

Esta tesis aborda dos problemas diferentes con un nexo en común: ambos son estudios experimentales donde el efecto de la gravedad no juega un rol importante. El primer problema se estudia en condiciones de microgravedad. En el segundo, la aceleración será mucho mayor que la de la gravedad. Por tanto, esta tesis se dividirá en dos partes: el crecimiento de burbujas en un líquido sobresaturado de gas en condiciones de microgravedad y la salida súbita de una placa circular sobre una superficie de agua.

En la primera parte, se estudia el crecimiento difusivo de una nube densa de burbujas en un líquido sobresaturado de gas en condiciones de microgravedad. Entender la dinámica de los mecanismos difusivos es relevante para varias tecnologías, como la fabricación espacial o en procesos químicos, así como en la formación de los pequeños cuerpos planetarios en geológia. Sin embargo, no es posible observar este crecimiento puramente difusivo durante más de 100 ms en condiciones normales. Por ello, hemos llevado a cabo una serie de experimentos en los que una nube de burbujas crece por difusión en un agua sobresaturada de CO_2 en microgravedad en la torre de caída del Centro Alemán de Tecnología Espacial Aplicada y Microgravedad (ZARM). En estos experimentos, se puede observar la evolución de la nube de burbujas durante más de 3 s, junto con sus interacciones y la competición entre ellas para acceder al CO_2 disponible en el líquido. Primero, se describe la configuración experimental diseñada y puesta en marcha para realizar los experimentos junto con algunos resultados preliminares acerca del crecimiento individual de burbujas grandes y la evolución del volumen de gas de la nube. Más adelante, mostramos la existencia de varios regímenes donde la nube de burbujas presenta diferentes ratios de crecimiento en nuestros experimentos. Finalmente, presentamos un modelo simplificado que describe estos regímenes y su índice de crecimiento correspondiente, de forma cualitativa.

En la segunda parte, estudiaremos experimentalmente la salida súbita de un disco circular situado en la superficie del agua. En ingeniería naval y oceánica, resulta esencial modelar la fuerza que debe soportar una estructura cuando impacta o sale del agua. Puesto que las simulaciones numéricas a gran escala generalmente no son prácticas para este propósito, a lo largo de los años se han desarrollado varios modelos analíticos o semianalíticos. Debido a la complejidad de los flujos de superficie libre involucrados, tanto los cálculos numéricos como los analíticos deben validarse experimentalmente. Con esta idea en mente, presentamos los resultados obtenidos de las medidas experimentales de la fuerza hidrodinámica que actúa sobre una placa que se levanta de la superficie del agua y que comienza a moverse hacia arriba repentinamente a una aceleración mucho mayor que la gravedad, $a \gg g$. Además, incluiremos el efecto hidroelástico observado en los experimentos en la solución del problema asimétrico de salida rápida del agua. Nuestro trabajo se centra en los primeros instantes del movimiento de la placa, cuando la succión y las fuerzas de inercia son las más relevantes. Por lo tanto, se describirá la configuración experimental, luego compararemos los resultados experimentales con la teoría linealizada del problema de salida rápida del agua propuesta por Korobkin (2013).

Finalmente, como consecuencia de las observaciones experimentales acerca de la interación hidroelástica entre el disco y el líquido, el problema de salida rápida del agua se reformula y se resuelve teniendo en cuenta este efecto.

Contents

Part I

Growing bubbles in a supersaturated liquid in microgravity conditions

CHAPTER 1

Introduction

The dynamics of a wet foam or a dense bubble cloud immersed in a gas-supersaturated medium are mainly determined by the diffusion of the dissolved gas towards the bubbles and by the advective transport of both the bubbles and the dissolved gas due to the flow induced by bubble growth. If the evolution of the foam or cloud takes place in a gravity field, the buoyancy of the bubbles will also play a, likely crucial, role in these dynamics. Even in the absence of buoyancy effects, the diffusion-driven growth of a cloud of bubbles is a rich problem in itself as a consequence of the complex interaction between the cloud components, which compete for the available dissolved gas to grow (or to dissolve, in case the liquid is undersaturated, as considered by Michelin *et al.* (2018)).

Besides the fundamental interest of this problem, the diffusive-driven dynamics of a cloud of bubbles (or drops) have received lately a renewed attention due to their applications in modern chemical processes such as solvent extraction Peng *et al.* (2018) and nanoscience Zhu *et al.* (2018). In these situations, as in many other applications on Earth, the only way to prevent bubbles from rising is to keep them pinned to a substrate. However, the pinning introduces additional complexities that obscure, to some extent, diffusive effects.

Unfortunately, a free bubble cloud in the Earth's gravity field exhibits a purely diffusion-driven growth only for a limited time, even for high gas concentrations such as those found for instance in beer or champagne, as shown by Rodríguez-Rodríguez *et al.* (2014). In this study, a dense bubble cloud was produced in the bulk of a CO_2-saturated liquid (beer) and its evolution recorded with high-speed imaging. This evolution could be divided into three stages: in a first one, which lasts about 10 ms, the size of the bubbles increases with the square root of time, as predicted by the Epstein-Plesset equation for the case of a single isolated bubble (Epstein & Plesset, 1950). Thus, it is reasonable to assume that in this stage bubbles grow without interacting much with each other. Then, another stage follows where bubbles moderate their growth, due to the depletion of the dissolved gas in the space between bubbles. These two stages, where the dynamics are driven by diffusive bubble growth, come to an end when gravity effects become important, which occurs as early as about 100 ms even for a bubble cloud with a size as small as about 1 mm.

Even in the case of a cloud of sessile bubbles in CO_2-supersaturated water, Enríquez *et al.* (2014) and Soto *et al.* (2019) have shown that, although in this case bubbles do not translate, the depletion of CO_2 that takes place around the bubble induces density gradients in the liquid that ultimately trigger a convection plume, which in turn dominates the flow and overcomes

the effect of diffusion.

These studies suggest that to investigate experimentally the diffusive interaction of free growing bubbles for a relatively long time requires avoiding the effect of gravity, that is, observing the bubble cloud growing in microgravity conditions.

In addition to the interest of the problem from a purely fundamental point of view, there are situations in which the diffusive growth of bubble clouds or wet foams takes place in microgravity or at least in reduced gravity conditions.

For example, in the field of planetary physics, the diffusive growth of bubbles is responsible for the lost of Helium in meteorites Stuart *et al.* (1999). Modeling the evolution of Helium content in these objects is important to understand the history of the formation of our solar system. Also in the Moon, rocks with a highly vesicular structure, such as the "Seatbelt Rock", have been found (see figure 4 in Jolliff & Robinson (2019)). This structure suggests that the rock has formed by solidification of a dense cloud of bubbles containing volatile gases, as a result of ancient volcanism.

From a more technological point of view, the behavior of foams in reduced gravity conditions is of interest for the development of advanced manufacturing processes in space, as pointed out by Koursari *et al.* (2019). These authors study experimentally the drying of a wet foam in the absence of gravity. Since gravity is essential to drain out the water filling the interstices between bubbles, they use a porous medium to soak up the liquid. Note that, if bubbles were allowed to grow, their motion would push out the interstitial water without the need for an external absorbing body.

Motivated by the above ideas, we have carried out experiments in which dense bubble clouds grow in CO_2-supersaturated water in microgravity conditions to explore the diffusion-driven growth experimentally at times much longer than in normal conditions on Earth. These experiments were performed in the drop tower of the German Center of Applied Space Technology and Microgravity (ZARM). It is worth pointing out that the void fractions explored here are smaller than those found in foams, which have been studied in the past in microgravity conditions both theoretically (Cox & G.Verbist, 2003) and experimentally (Saint-Jalmes *et al.*, 2006). Also the behavior of plateau borders, where the interfaces of adjacent bubbles meet, has been studied in the absence of gravity (Barrett *et al.*, 2008). Although studying cavitation is not the main purpose of the experiment, we exploit this phenomenon to generate the bubble cloud. Cavitation in a microgravity environment was explored experimentally by Obreschkow *et al.* (2011). In their experiments, they induced cavitation by focusing a laser pulse in the bulk liquid, whereas here we use a spark for that purpose. However, the main difference is that in the work by Obreschkow *et al.* (2011) the gas cavity disappears upon its collapse, whereas here the bubble fragments that result from the collapse become the nuclei from which the bubbles in the cloud will grow. This different behavior occurs because the water that we use is supersaturated, i.e. contains more CO_2 than what the liquid can dissolve, thus this gas fills the cavitation fragments and precludes their dissolution. Moreover, inspired by our experimental results, we have put together a mathematical model of the growth of a bubble cloud in a gas-supersaturated solution that is able to explain, albeit in a qualitative fashion, the different stages observed in the experiments.

Attending to these ideas, this part of this thesis is organized as follows. In §2 we describe the experimental set-up as well as the preliminary results regarding the individual growth of large bubbles and the evolution of the gas volume of the cloud using the mean grey level of the images. In §3, we present experiments where a dense bubble cloud grows

by diffusion in microgravity conditions thus the collective effects between bubbles can be observed. Furthermore, we propose a mathematical model that reproduces, in a qualitative way, the behavior of the growth rate observed in the experiments. Finally, in §4 we summarize the main conclusions of this work.

CHAPTER 2

Drop Tower setup to study the diffusion-driven growth of a bubble cloud in supersaturated liquids in microgravity conditions

The diffusion-driven growth of a foam ball is a phenomenon that appears in many manufacturing process as well as in a variety of geological phenomena. Usually these processes are greatly affected by gravity, as foam is much lighter than the surrounding liquid. However, the growth of the foam free of gravity effects is still very relevant, as it is connected to manufacturing in space and to the formation of rocks in meteorites and other small celestial bodies. The aim of this research is to investigate experimentally the behaviour of a bubble cloud growing in a gas-supersaturated liquid in microgravity conditions. Here, we describe the set-up used to perform this experiment in the drop tower of the Center of Applied Space Technology and Microgravity (ZARM). In few words, a foam seed is formed with spark-induced cavitation in carbonated water, whose time evolution is recorded with two high-speed cameras. Our preliminary results shed some light on how the size of the foam ball scales with time, in particular at times much longer than what could be studied in normal conditions, i.e. on the surface of the Earth, where the dynamics of the foam is already dominated by gravity after several milliseconds.

2.1 Experimental set up

The goal of this experiment is to study the diffusion-driven growth of a bubble cloud in a CO_2-supersaturated water at longer times than a few hundreds of milliseconds, when gravity becomes dominant in normal conditions on Earth. The experiment consists on the formation of a bubble cloud in a gas-supersaturated liquid by spark-induced cavitation. We then, observe the development of the cloud using high-speed imaging in microgravity conditions.

To achieve this aim, we performed experiments in the drop tower facility at the German Center of Applied Space Technology and Microgravity (ZARM). The drop tower consists of a tube of 146 m of total height, where an encapsulated experiment is dropped from 120 m. After 4.72 seconds of free fall, the capsule is decelerated and stopped in a pool filled with polystyrene pellets. Before dropping the capsule, the drop tube must be empty of air. For

that, several pumps work for around 30 minutes to remove the air inside the tube, while the experiment waits at the top (FABmbH & Fallturm, 2010).

Here, we describe the set-up designed and built for the two experimental campaigns carried out. This set-up was designed following the directions given by FABmbH & Fallturm (2008). During the first campaign, we detected a few issues that have been solved in the second campaign. The modifications and enhancements are detailed below as well.

2.1.1 General set up

Figure 2.1 shows the layout of the experimental setup and the drop tower facility. The measurement chamber, where the bubble cloud evolves, is the main component of the experiment. Its body is a cylinder of Pyrex glass that contains CO_2-supersaturated water. Around the cylinder there is a rectangular prism that is filled with degassed water. The purpose of this jacket is to avoid the optical aberration caused by a cylindrical container. At the top of the tank, there is a line which is connected to a pressurized CO_2 gas bottle through an electrovalve (V_1). In this line, there are two more electrovalves (V_2 and V_3) that connect the chamber to the ambient to depressurize the chamber. Downstream of the electrovalve V_2 there is a reduction valve to achieve a smoother depressurization of the tank before the experiment starts. This is necessary since abrupt depressurization induces bubble growth at unwanted locations in the measurement tank. A pressure sensor (Gems, 220RAA6002F3DA, 0-6 bar) controls the pressure during the pressurization and depressurization of the chamber. Near the bottom of the measurement chamber, there are two copper filaments of 100 μm in diameter. These thin naked copper wires are used as electrodes, that are connected to the spark generator device that discharges a large capacitor in a very short time ($\sim$400 μs). The spark generator reproduces the discharge circuit described in Willert *et al.* (2010) but replacing the LED by the electrodes, as suggested by Goh *et al.* (2013). A capacitor (2200 μF) is charged through a power supply (30–35 V) and is discharged thought a fast MOSFET power transistor when it receives a TTL trigger signal. This discharge induces cavitation, and the collapse of the imploding bubble generates the bubble cloud, which is the target of the experiment. Figure 2.2 shows pictures of the real look of experiment inside the capsule.

The supersaturated liquid has been prepared in the installation designed by Enríquez *et al.* (2013) at the University of Twente. In this way, we can control the saturation level of the liquid. However, the solution is brought in bottles to ZARM and due to the manipulation during the filling of the measurement tank, the CO_2 concentration is lower than the initial concentration in the preparation.

In order to measure the time evolution of the total volume of exsolved gas in the measurement chamber, the following system has been designed. At the top of the measurement chamber, a capillary tube connects a second gas-filled vessel that works as an expansion tank. This allows the free expansion of the liquid-gas mixture during the experiment. As the bubble cloud grows inside the liquid, the free surface advances into the measurement line thus compressing the gas inside. It is easy to see that the overpressure satisfies $\left|\frac{\Delta P}{P_0}\right| \simeq \left|\frac{\Delta V}{V_0}\right|$, where P_0 is the initial pressure in the line (ambient), ΔP is measured by a differential pressure sensor (Sensirion, $SDP610 \pm 25Pa$), V_0 is the initial gas volume in the line and ΔV is the volume of the exsolved gas. In the same line, we place an expansion vessel with a relatively large volume V_0 ($\sim 5\ ml$) to act as a buffer, since the determination of the initial gas volume in the line is not feasible. Unfortunately, we anticipate that these pressure measurements obtained are useless due to the high level of noise (see § 2.2.2).

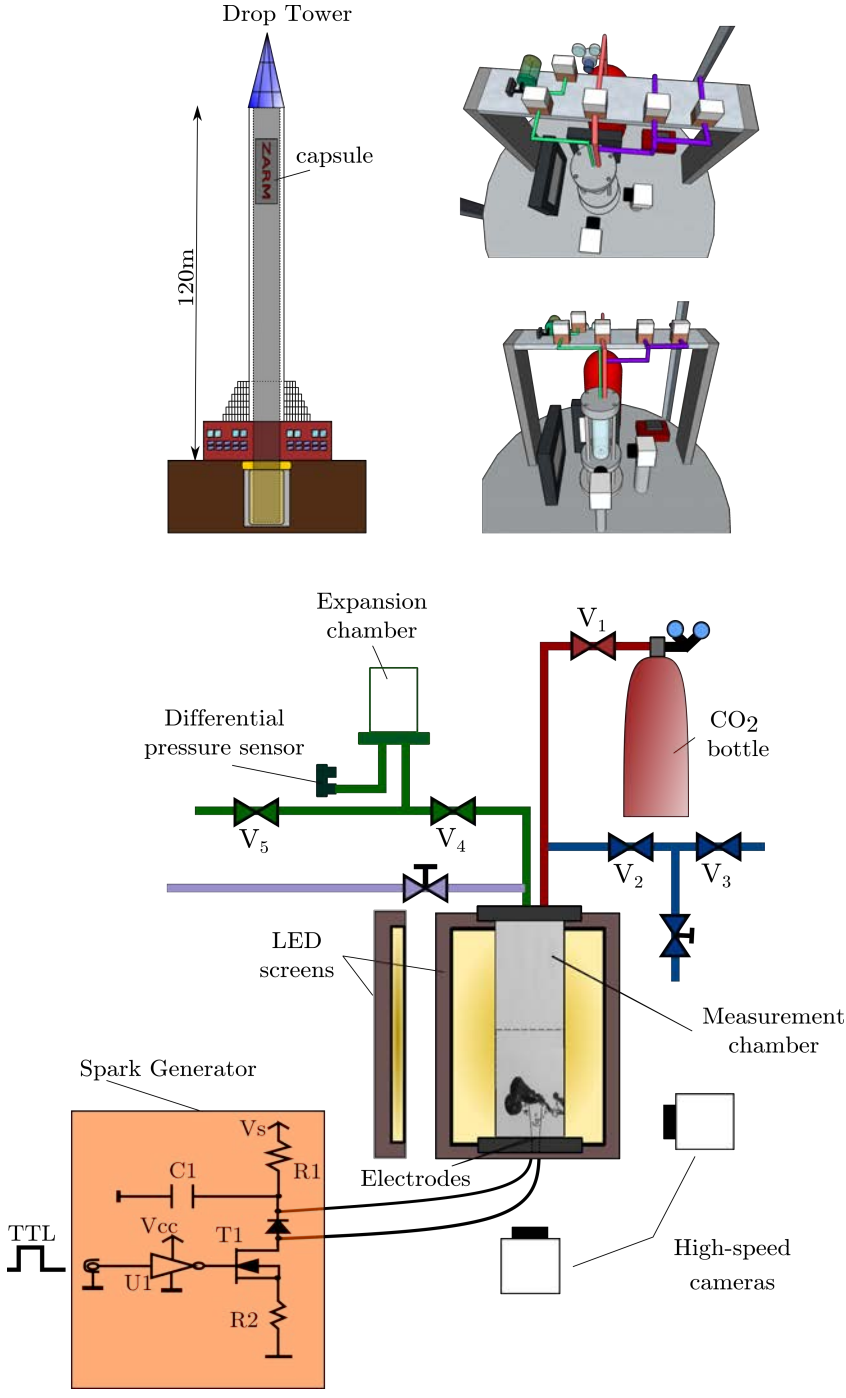

FIGURE 2.1. Layout of the experimental setup in 3D and 2D and the drop tower facility. The electronic components of the Spark Generator are: a capacitor, C1 = 22000 μF, a diode, D1 = BYT01-400, a MOSFET, U1 = UCC37322P, a transistor, T1 = IRFB3206GPbF, and the resistances, R1 = 1-2 Ω and R2 = 0.002 Ω.

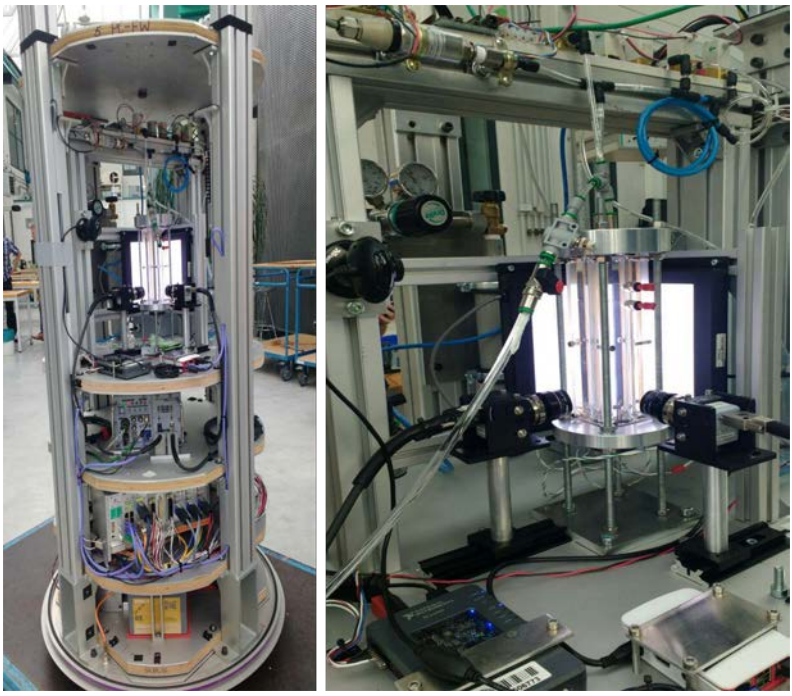

FIGURE 2.2. Photos of the experiment inside the capsule.

2.1.2 Experimental procedure

Before filling the measurement chamber with carbonated water, we flush the chamber and the electrodes with alcohol to reduce bubble formation at the walls. The electrodes are in contact inside the tank and connected to the *Spark Generator* device. Initially, all the electrovalves are closed. Then, electrovalve V_1 is opened and the CO_2 gas fills up the measurement vessel up to about the same pressure that we carbonated the water. The purpose is to dissolve all the bubbles that may have appeared in the chamber during its filling. After approximately 30-40 minutes, while the pumps of the tower evacuate the air inside the drop tube, the electrovalve V_1 is closed. Now, electrovalve V_2 is opened, thus exposing the chamber at ambient pressure, half a second after the V_5 are opened too, hence the pressure in the expansion tank will be at ambient pressure. After that, V_3 is closed and V_4 is opened (see figure 2.3). Then, a TTL signal triggered the differential pressure sensor and the high-speed cameras a few milliseconds before the spark. Then, when the capsule achieves microgravity conditions during its drop, the spark is triggered and a bubble cloud is generated. At this point, the experiment starts.

2.1.3 Improved experimental setup

Although we obtained good results in the first campaign, we had two main issues: (*i*) a bubbly jet forming at the surface during the pressurization time that penetrated down where the bubble cloud was formed due to a spark, and (*ii*) the carbonated water was brought in bottles from the University of Twente to fill the measurement chamber and during its

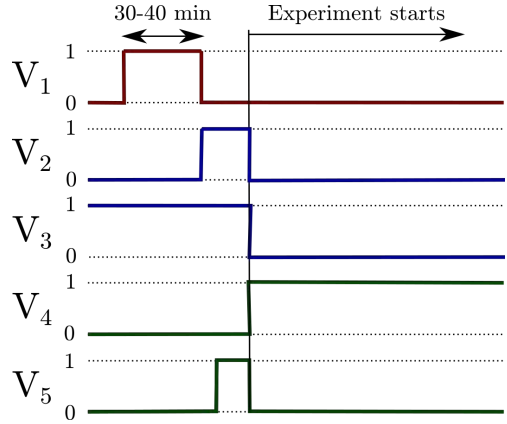

FIGURE 2.3. Valve-sequence diagram followed in the experimental procedure, where 1 means opened, and 0 closed.

manipulation we lost a significant amount of CO_2 in the water. Hence, we could not explore the bubble-bubble interaction effects because the gas saturation level was lower than we expected. In this second experimental campaign, we modified the experimental set-up to solve these problems. Firstly, we modify the height of the measurement chamber to avoid the effect of the bubble jet generated during the depressurization time. Now, the measurement chamber has a similar diameter of 24.4 mm and a height of 200mm, which is twice the height of the previous campaign. In this way, the bubble jet is generated far away from our point of interest where the spark produces the bubble cloud. Furthermore, we built a device to produce carbonated water on-the-site and then transfer the water to the measurement chamber under pressure, thus no gas was lost during the process (see figure 2.4). This apparatus is based on the experimental installation described by Enríquez *et al.* (2013). In few words, this facility degasses deionized water through a degass cell (Membrana, 0.75 x 1 MicroModule) and a vacuum pump. The degass deionized water is mixed with CO_2 gas at a fixed pressure, around 4 or 5 bar in our case, using a magnetic stirrer. In this way, we reach a high supersaturation level, $\zeta \sim 3$–4, to explore the regime where bubbles grow by diffusion for longer times and observe the collective effects between bubbles, which will be discussed in §3.

Figure 2.5 compares the evolution of a bubble cloud from its generation (the spark) to the end of the experiment, approximately 3.4 seconds later in 1-g conditions and in microgravity using the original setup (June 2016) as well as its improved version (June 2018). All tests show a diffusion-driven growth during the first 100 ms. On the one hand, the effects of the gravity become visible in the 1-g test: the cloud starts a buoyancy-induced rising motion as can be seen in the first row of the figure 2.5. On the other hand, in the microgravity tests, the bubble cloud continues its growth by diffusion. The microgravity test done in 2016 shows a bubble cloud with some scattered bubbles due to the gas lost during the filling process. The motion observed in this test is a consequence of the residual velocity as a result of the implosion. Despite the problems in this campaign, we got relevant information regarding the diffusion-driven growth detailed below in §2.2. By contrast, a dense bubble cloud is shown in the test carried out in 2018 using the improved setup, where the bubble cloud continues growing by diffusion and no net motion is observed. Besides, the collective effects between bubbles are visible due to the high level of CO_2 in the water. These observations are one of

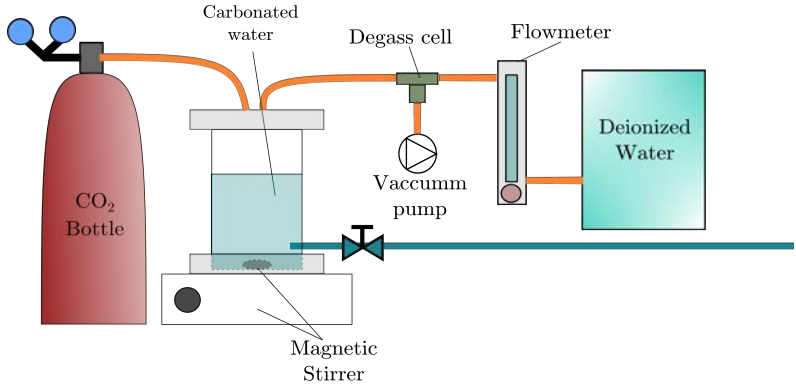

FIGURE 2.4. Sketch of the carbonator to produce CO_2-saturated water *in situ*.

the motivations for the mathematical model developed in §3.

2.2 Preliminary results

We report in this section preliminary results on the growth rate of the radius of the individual bubbles, the 3D reconstruction of the structure of the cloud and the time-evolution of the total gas volume in the cloud. The latter is obtained through the analysis of the mean grey level of the images, which will allow us to determine quantitatively the time evolution of the cloud's volume. The purpose of this section is to illustrate the kind of quantitative information that can be obtained with the experimental set-up described previously (§ 2.1.1). The drops whose results are shown in figures 2.6, 2.7 and 2.9 were carried out between June 27$^{\text{th}}$ and July 1$^{\text{st}}$, 2016 (first campaign).

2.2.1 Radial expansion of individual bubbles

We start from the well-known Epstein–Plesset equation (Epstein & Plesset, 1950; Brennen, 1995). It describes the growth rate of the bubble radius as a function of the properties of the gas and the level of saturation in the liquid. For our purpose, it is useful to rewrite it in terms of the square of the radius. Thus, after some mathematical manipulations we obtain:

$$\frac{1}{2}\frac{dR^2}{dt} = D\frac{\Delta C}{\rho_g}\left(1 + \frac{R}{\sqrt{\pi D t}}\right), \tag{2.1}$$

where D is the diffusivity of CO_2 in water, ρ_g the density of the gas inside the bubble and ΔC the difference in concentration of CO_2 between the bubbles in the surface and the bulk fluid. Numerical integration of equation (2.1) reveals that, for times of the order of R_0^2/D or longer, with R_0 the initial bubble radius, the second term in the right hand side of equation (2.1) approaches a constant (Epstein & Plesset, 1950), thus the square of the radius grows linearly with time:

$$R^2 \sim F\left(\frac{\Delta C}{\rho_g}\right) Dt = F\left(\Lambda(\zeta - 1)\right) Dt, \tag{2.2}$$

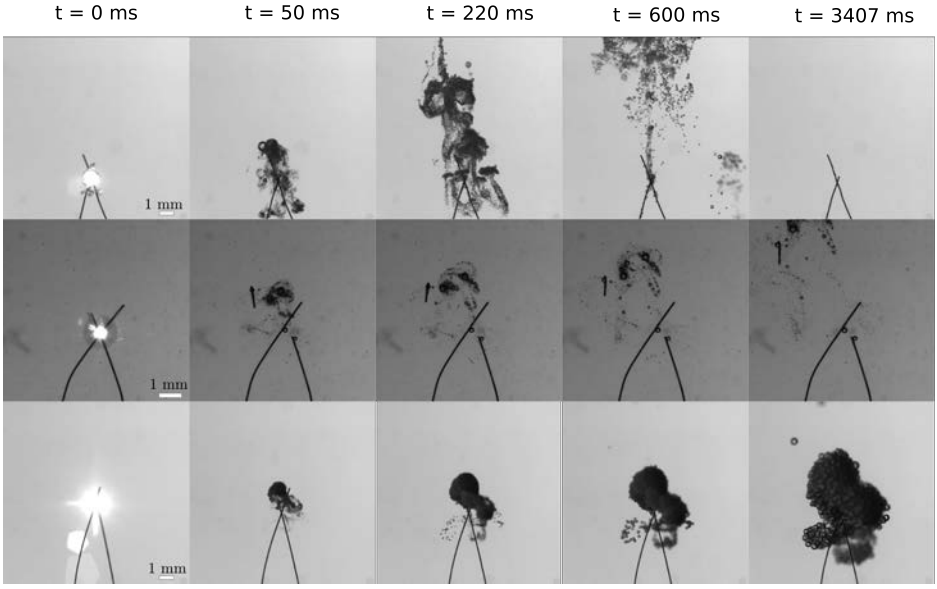

FIGURE 2.5. Comparison of experiments where the bubble cloud develops with and without gravity.

where $\Lambda = K_h R_g T_\infty$ is the Ostwald coefficient, K_h is Henry's constant, R_g the gas constant and T_∞ the temperature. Physically speaking, Λ is a constant which measures the gas solubility. In the parenthesis, ζ is the supersaturation level which measures the amount of dissolved CO_2 available for bubble growth. The function $F(x)$ is given by:

$$F(x) = \frac{x}{\sqrt{\pi}} + \sqrt{\frac{x^2}{\pi} + 2x}. \tag{2.3}$$

Note that, in these calculations, the effect of surface tension on the gas pressure has been neglected, as bubbles are much larger than $2\sigma/P \approx 0.8$ μm, the size at which capillary overpressure, $2\sigma/R_0$, becomes equal to the ambient one, P. Indeed, taking $\sigma = 0.0434$ N/m, the Laplace overpressure is at most about 2% of the ambient one even for the smallest bubbles reported here.

To measure the growth of the bubble radius in the experiments, we track individual bubbles in the cloud using custom-made image processing software implemented in Matlab. The time evolution of the bubble radii for different bubbles in the same experiment is shown in figure 2.6. In some experiments, bubbles are attached to the electrodes. We consider these bubbles to be isolated as they are far away from others whereas the area in touch with the electrode is small. Consequently, their growth rate gives us an estimation of the saturation level (see figure 2.6). Indeed, the growth rates of the squared radius of the bubbles considered as isolated are around three times larger than those of bubbles found inside the cloud. Moreover, the growth rate of the bubbles on the electrodes are nearly the same, whereas in contrast, growth rates for the bubbles inside the cloud differ in a visible way (see figure 2.6). This variability of growth rates is consistent with the fact that these bubbles compete for the available CO_2 in their surroundings and this competition for the CO_2 provides information about how an individual bubble interacts with the rest of the bubbles in the cloud.

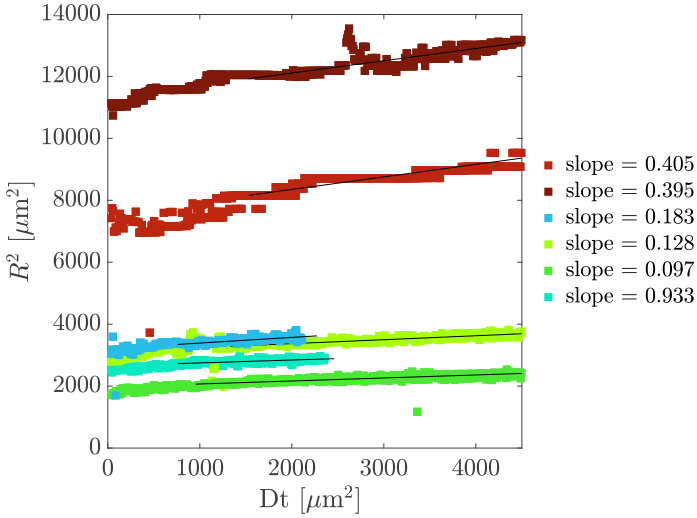

FIGURE 2.6. Time evolution of the squared radius of different bubbles in the experiment. The red square symbols represent the evolution of two bubbles attached to the electrodes as Figure 2.5 shows in the pictures of the second row, and which can be considered as isolated, while the bluish square symbols show the evolution of several bubbles inside the cloud.

In order to get quantitative data to validate future models of bubble cloud growth, we take advantage of the fact that the experiment uses two high-speed cameras forming a 90^o angle to reconstruct the 3D structure of the cloud (see figure 2.7 for an example). This information will allow us to relate the local level of saturation with the position of the bubble in the cloud.

2.2.2 Determining the gas volume of the cloud

Although tracking individual bubbles yields very useful quantitative information, this technique can only be applied to relatively large bubbles. Nonetheless, a significant volume of the cloud corresponds to very fine and small bubbles that lie below the spatial resolution of our high-speed cameras. Thus, to determinate the time evolution of the total gas of the cloud we installed the differential pressure sensor, however it does not have the results that we expected it, so as an alternative way we analyze the mean grey level of the images.

Pressure measurements

As we said in § 2.2.2, it would be easy to relate the pressure measured by the sensor with the exsolved gas. In normal gravity conditions, a bubble cloud is formed that grows due to diffusion and buoyancy-driven advection as explained in Rodríguez-Rodríguez *et al.* (2014). As the cloud volume increases, the liquid surface compresses the air inside the expansion tank as shown in figure 2.8a. Interestingly, after $t \approx 3.5$ s the pressure decreases, coinciding this with the moment when the bubble cloud reaches the liquid free surface. The decrease of the pressure is due to the fact that the differential pressure sensor allows some gas to flow through it to the ambient, since it measures the pressure difference precisely based on this flow Homan *et al.* (2014). In microgravity conditions, we are not capable to measure the pressure due to the noise occurring inside the chamber and tubes as shown in figure 2.8b. There are too many

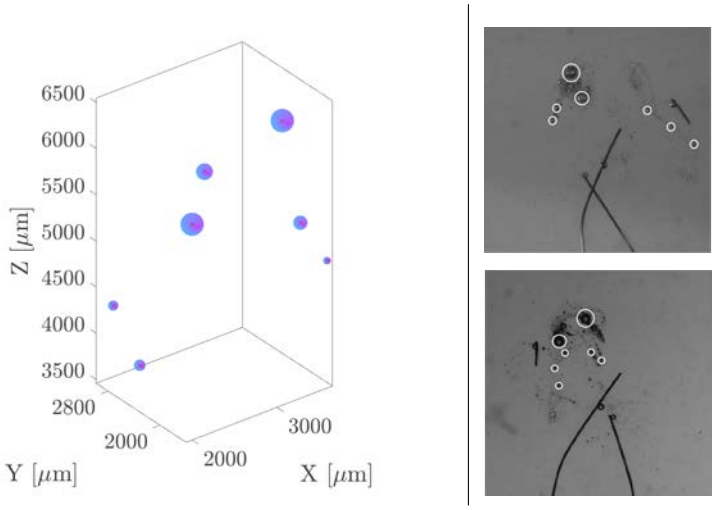

FIGURE 2.7. Using digital image processing, we detect the position of large bubbles at each instant of time in the images of the two cameras. This allows us to detect reconstruct the 3D structure of the bubble cloud, or at least of those bubbles large enough to be tracked.

peaks and it is impossible to identify which one corresponds to the bubble cloud under these conditions since the volume of gas is less than in 1-g conditions where the gravity makes the bubbles grow faster. Note that in normal gravity conditions the over pressures are much larger the most of the peaks in microgravity.

Mean grey level of the images

As an alternative way to determine the time evolution of the total gas volume of the cloud, we analyze the mean grey level of the images. This mean grey level, MGL, can be defined as

$$MGL = \frac{\sum_{i=1}^{H}\sum_{j=1}^{W} Im_{i,j}}{HW}, \tag{2.4}$$

where H and W are the height and width of the image matrix, Im, respectively. Next, we must establish a relation between this mean grey level and the volume, in other words, we must obtain a calibration curve. This can be done by generating a bubble cloud with a well-controlled volume via electrolysis.

Indeed, using Faraday's law for electrolysis (Ehl & Ihde, 1954; Strong, 1961), we are able to predict the volume of the gas generated as the current flowing through the electrodes is known. The expression of the Faraday's law for electrolysis is

$$m = \left(\frac{Q}{F}\right)\left(\frac{M}{z}\right), \tag{2.5}$$

where m is the mass of the substance liberated at an electrode, Q is total electric charge that has flowed through the electrolyte (the liquid), and that can be obtained as the time integral of the current; $F = 96500\ \mathrm{C{\cdot}mol^{-1}}$ is Faraday's constant, M is the molar mass of the gas

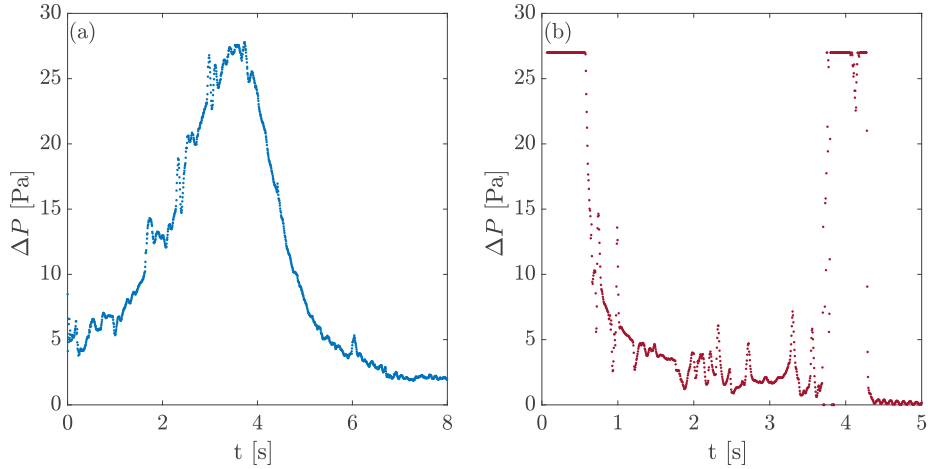

FIGURE 2.8. Pressure measurement taken with the Sensirion SDP610 125Pa differential sensor in the measurement chamber in (*a*) 1-*g* and in (*b*) microgravity conditions.

(Hydrogen in our case) and z is the number of electrons transferred per ion. The mass, m, divided by the molar mass, M, is the number of moles, n. In order to obtain the volume, V, we use the ideal-gas law $PV = n\bar{R}T_\infty$ where, P is the pressure of the gas (nearly ambient here), $\bar{R}$ is the universal gas constant and T_∞ is the temperature. Thus, we carried out calibration experiments producing bubble clouds by electrolysis in the same experimental chamber used for the drops. The procedure was the following: the measurement chamber is filled up with clean water and the electrodes are separated and connected to a current source. This produces a known volume of gas which is then filmed with the high-speed camera. In order to measure the current in the circuit, a resistor ($\Omega_c = 18\Omega$) is placed in series with the electrodes. The voltage across the resistor is measured with an oscilloscope. We use deioned water to which a small amount (15 grams per liter) of potassium carbonate was added in order to make it conductive (Medina-Palomo, 2015). The overall reaction of the electrolysis of the water is

$$2H_3O^+ + 2e^- \longrightarrow H_2(g) + 2H_2O, \tag{2.6}$$

so, z will be equal to 2 (Harrison & Levene, 2008).

We show the mean grey level of the images with the volume produced by electrolysis at different voltages (see figure 2.9a). The mean grey level increases linearly with the volume. Moreover, the curves for the different voltages and different experimental realizations (3 per voltage) overlap, which proves the reliability of the results. Indeed, although the bubble size distributions show some variation for the different voltages, these changes do not affect the calibration curve. It should be pointed out that, in the calibration curves (figure 2.9a) the first tens of milliseconds upon starting electrolysis have been excluded, since at those early times the Hydrogen has remained in dissolution and does not form bubbles.

Therefore, making use of the calibration curve obtained, the time evolution bubble cloud volume evolution in the drops can be estimated with the analysis of the mean grey level. As an example, figure 2.9b shows the evolution of the mean grey level and the volume for drop $N°4$ of the first campaign.

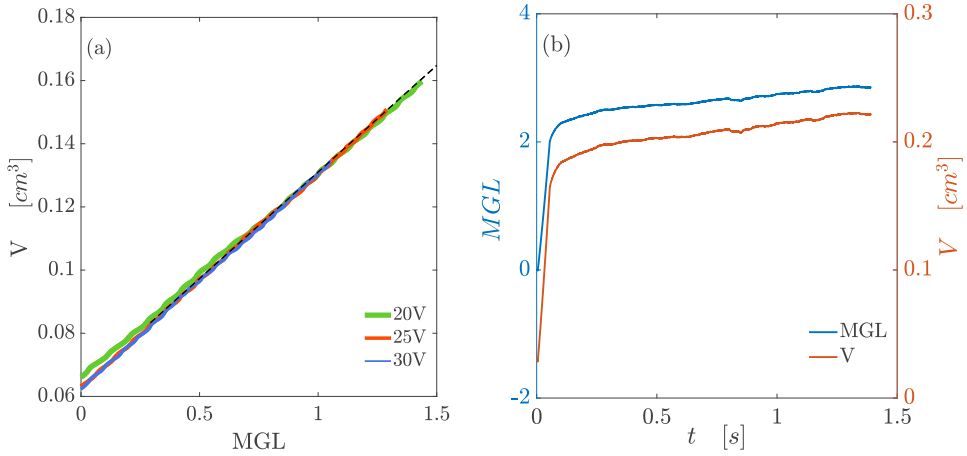

FIGURE 2.9. Plot (a) represents the relation between the mean grey level and the gas volume generated by electrolysis at different voltages, namely 20 V, 25 V and 30 V, P = 1 atm and T = 288 K. The dashed line shows the calibration curve. In plot (b), the blue solid line presents the time evolution of the mean grey level of one experiment and the orange dashed line shows the time evolution of the gas volume calculated according to the calibration curve. In both plots, the data has been filtered using a moving average filter to remove high-frequency noise.

Acknowledgements

This work was supported by the Netherlands Center fro Multiscale Catalist Energy Conversion (MCEC), an NWO Gravitation programme funded by the Ministtry of Education, Culture and Science of the goverment of the Netherlands and the Spanish Ministry of Economy and Competitiveness though grants DPI2014-59292-C3-1-P and DPI2015-71901-REDT, partly funded through European Funds. We thank the team from the ZARM Drop Tower Operation and Service Company (ZarM FAB mbH) for valuable technical support during the experimental campaigns. The technicians from Universidad Carlos III for their technical labor during the built of the experimental set up. The European Space Agency (ESA) is acknowledged for provinding access to the Drop Tower through grants HSO/US/2015-29/AO and HRE/RS-PS/2018-7/AO.

CHAPTER 3

Growth of a bubble cloud in CO_2-saturated water in microgravity

The diffusion-driven growth of a dense cloud of bubbles immersed in a gas-supersaturated liquid is a problem that finds applications in several modern technologies such as solvent-exchange micro-reactors, nanotechnology or the manufacturing of foamy materials. However, under Earth's gravity conditions, these dynamics can only be observed for a limited time if the cloud is not attach to a surface, due to the quick action of buoyancy, i.e. of gravity effects. Here, we present experimental observations of the time evolution of dense bubble clouds growing in CO_2-supersaturated water in microgravity conditions. We report the existence of three different regimes where the bubble cloud exhibits likewise different growth rates. At short times, each bubble grows independently following the Epstein–Plesset equation. Later on, they start to interact with each other and their growth rate diminishes as they compete for the available CO_2. When this happens, the bubble growth slows down earlier the deeper they are in the cloud and, at long times, only those on the husk continue growing. These regimes are qualitatively described by a mathematical model where each individual bubble grows in the presence of a constellation of point mass sinks. Despite the model, strictly speaking, being only valid for dilute bubble clouds, its predictions agree fairly well with the experimental observations, even though the bubble clouds we observe are rather dense. We expect our model to shed light on the competition dynamics of a population of particles, bubbles in our case, which compete for an available resource.

3.1 Experiments

We carried out experiments to observe the diffusion-driven growth of a dense bubble cloud immersed in a supersaturated liquid, in our case CO_2-saturated water, and their interactions using high-speed imaging in microgravity conditions. In this campaign we use the improved set-up describe in §2, section 2.1.3. This experiment is encapsulated at ambient pressure and dropped inside the drop tower of the German Center of Applied Space Technology and Microgravity (ZARM). Figure 3.1 shows screenshots of one experiment of those experiments from two perpendicular views recorded by the high-speed cameras at 2000 fps. In these sequences the purely diffusion growth of the bubble cloud can be observed from the generation

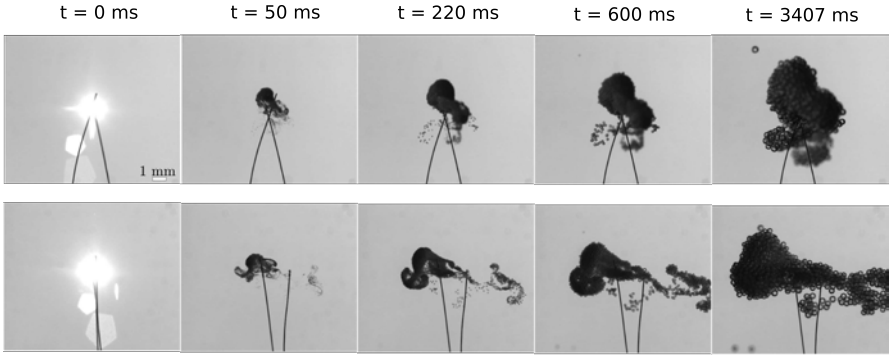

FIGURE 3.1. Both views of one experiment at different times from its generation to the end of the experiment at 3.4 s.

of the cloud (the spark) to the end of the experiments, around 3.4 second later. Besides, no net motion as well as the irregular shape of the cloud is observed.

Despite we get information of two views to measure the evolution of the shape and the size of the cloud, the high bubble density of the cloud precludes the observation of its interior. Consequently, it is not possible to determine experimentally the number of bubbles nor its size distribution, at least not accurately. However, when the capsule brakes upon reaching the bottom of the tower, the sudden appearance of a large apparent gravity allows us to momentarily observe those bubbles that were at the center of the cloud (see figure 3.2). This observation reveals that bubbles deep inside the cloud are much smaller than those near the outer edge. The model put forward next explains this as a consequence of the depletion of available CO_2 that occurs inside the cloud. Besides, it is important to point out that, despite the high bubble density of the cloud, very few bubbles coalesce during the experiments. Thus, in the first approximation, its number may be regarded as constant.

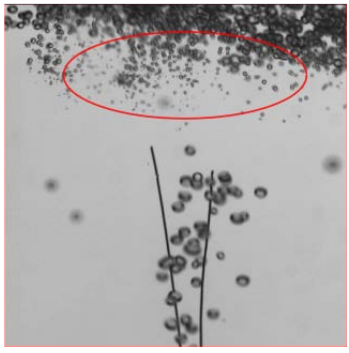

FIGURE 3.2. Snapshot of a high-speed movie showing the cloud during the deceleration of the capsule ($\zeta \sim 4$). As the capsule comes to a stop, the large deceleration makes the bubble cloud rise fast. Because large bubbles rise faster, this allows us to see those that were inside the cloud (red region).

Another important aspect is to determinate the saturation level of CO_2 in the water in the experiments. The saturation level is defined by $\zeta = C_0/C_s$ where C_0 is the concentration in

the liquid far away from bubbles and C_s is the saturation concentration at the ambient pressure P_s, that is $Cs = k_H P_s$, k_H is the Henry's constant. Some isolated bubbles appear in almost all the experiments, so we use these bubbles to determinate the saturation level, ζ, in the same way of the growth rate of large individual bubble described in §2.2 in the previous chapter. To this end, we track the evolution of their radius with a custom-made algorithm implemented in Matlab and then, we estimate ζ using the Epstein-Plesset equation (Epstein & Plesset, 1950). The values of ζ vary between 3.5 and 4.3.

3.2 Mathematical model of transient mass transfer in a bubble cloud

Let us consider a spherical bubble of radius R_i surrounded by a cloud of other bubbles of radii R_j, with $j = 1, ..., N$ where N is the total number of bubbles in the cloud, and $j \neq i$. We introduce here two hypotheses. First, from the point of view of mass transfer, one bubble sees the others in the cloud as point mass sinks of intensity $\dot{m}_j$. Second, advective effects caused by bubble growth are neglected in the gas transport equation. This means that the concentration of dissolved gas, namely CO_2, obeys the heat equation. Due to the linear nature of this equation, the interaction of the i-th bubble with the surrounding ones can be treated by superposition. For this reason, we consider the growth of a bubble in presence of a point mass sink, of intensity $\dot{m}_j$, a distance d apart from the bubble center (see figure 3.3). The problem exhibits cylindrical symmetry around the line connecting the centers of both bubbles, so the concentration field obeys

$$\partial_t C - D\left[\frac{1}{r^2}\partial^2_{rr}\left(r^2 C\right) + \frac{1}{r^2 \sin\theta}\partial_\theta\left(\sin\theta \partial_\theta C\right)\right] = -\dot{m}_j \delta\left[\vec{x} - d\vec{e}_x\right]. \tag{3.1}$$

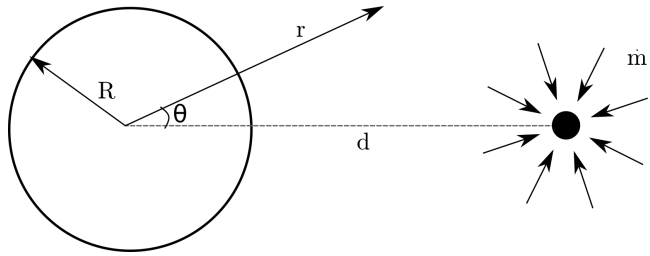

FIGURE 3.3. Bubble of radius R in the presence of a mass sink of intensity $\dot{m}$ located a distance d apart.

This equation must be subject to the boundary conditions at the bubble surface, $r = R$, and in the far field $r \to \infty$. At the bubble surface the concentration is given by Henry's law, in other words $C(R, t) = k_H P_\infty$, where k_H is the Henry's constant, whereas in the far field $C(\vec{x}, t) = C_\infty$. The solution will be sought by exploiting the linearity of the problem to decompose it into a spherically-symmetric one that satisfies these boundary conditions plus another one that accounts for the point sink but that has homogeneous boundary conditions. The former solution recovers the mass flux given by the Epstein–Plesset equation (Epstein & Plesset, 1950), $\dot{m}_{i0}$. In what follows we derive the later, $\dot{m}_{ij}$, also adopting the assumption underlying to the Epstein–Plesset equation that the radius of the bubble, R_i, is constant in time.

Transforming equation (3.1) into the Laplace plane, with $\hat{C}(r,s)$ and $\hat{m}_{ij}(s)$ the Laplace transforms of $C(r,t)$ and $\dot{m}_{ij}(t)$, respectively:

$$s\,\hat{C} - D\left[\frac{1}{r^2}\partial_{rr}^2\left(r^2\,\hat{C}\right) + \frac{1}{r^2\sin\theta}\partial_\theta\left(\sin\theta\partial_\theta\hat{C}\right)\right] = -\hat{m}_j\delta\left[\vec{x} - d\vec{e}_x\right]. \tag{3.2}$$

The general solution to this equation is (Wu, 2015):

$$\begin{aligned}\hat{C} = &-\frac{\hat{m}_j}{4\pi D}\frac{\exp\left(-\sqrt{s/D}\sqrt{d^2+r^2-2dr\cos\theta}\right)}{\sqrt{d^2+r^2-2dr\cos\theta}} + \\ &+\sum_{l=0}^{\infty}\left[a_l\,h_l^{(1)}(\sqrt{-s/D}\,r) + b_l\,h_l^{(2)}(\sqrt{-s/D}\,r)\right]\,P_l(\cos\theta),\end{aligned} \tag{3.3}$$

where $h_l^{(1)}$ and $h_l^{(2)}$ are Haenkel's functions of first and second kind, respectively. Although to compute the concentration field it is necessary to determine the full set of coefficients (a_l, b_l), the calculation of the mass flux that the sink induces on the bubble only requires knowledge of the coefficients a_0 and b_0. Indeed, the mass transfer due to higher-order harmonics is zero, as

$$\dot{m}_{ij} = -2\pi R^2 D\int_0^\pi \left.\frac{\partial C}{\partial r}\right|_{r=R}\sin\theta\,\mathrm{d}\theta \sim \int_0^\pi P_l(\cos\theta)\,\sin\theta\,\mathrm{d}\theta, \tag{3.4}$$

with the last expression being zero for $l \geq 1$. Moreover, the coefficient b_0 must vanish, as the function $h_0^{(2)}\left(\sqrt{-s/D}r\right)$ is unbounded as $r \to \infty$. Introducing (3.3) into (3.2) and projecting onto $P_0(\cos\theta)$ we get

$$\begin{aligned}0 = &-\frac{\hat{m}_j}{4\pi D}\int_{-1}^{1}\frac{\exp\left(-\sqrt{\frac{s}{D}}\sqrt{d^2+R^2-2dRx}\right)}{\sqrt{d^2+R^2-2dRx}}\,\mathrm{d}x + \\ &+2a_0h_0^{(1)}\left(\sqrt{-s/D}\,R\right),\end{aligned} \tag{3.5}$$

where the change $x = \cos\theta$ has been introduced. Evaluating the integrals, and taking into account $h_0^{(1)}(\sqrt{-s/D}\,R) = -e^{-\sqrt{s/D}\,R}/\sqrt{s/D}\,R$,

$$0 = \frac{\hat{m}_j}{4\pi D}\frac{2e^{-\sqrt{s/D}\,d}}{Rd\sqrt{s/D}}\,\sinh\left(\sqrt{s/D}\,R\right) + 2a_0\frac{e^{-\sqrt{s/D}\,R}}{\sqrt{s/D}\,R}, \tag{3.6}$$

thus

$$a_0 = -\frac{\hat{m}_j}{4\pi Dd}\,e^{-\sqrt{s/D}(d-R)}\,\sinh\left(\sqrt{s/D}\,R\right). \tag{3.7}$$

Introducing this value of a_0 together with $b_0 = 0$ into (3.3) and differentiating we get

$$\int_0^\pi \left.\frac{\partial\hat{C}}{\partial r}\right|_{r=R}\sin\theta\,\mathrm{d}\theta = -\frac{\hat{m}_j}{2\pi DdR}\exp\left(-\sqrt{\frac{s}{D}}\,(d-R)\right). \tag{3.8}$$

Transforming this expression back into the time domain and introducing it in the definition of the mass flux (3.4),

$$\dot{m}_{ij} = -\frac{R^2D}{2\sqrt{\pi}}\int_0^t\frac{1}{R}\left(1-\frac{R}{d}\right)\frac{\dot{m}_j(t')}{[D(t-t')]^{3/2}}\,\exp\left(-\frac{(d-R)^2}{4D(t-t')}\right)\mathrm{d}t'. \tag{3.9}$$

This expression must be added to the mass flux provided by the Epstein–Plesset equation, $\dot{m}_{i0}$, to yield

$$\dot{m}_i = 4\pi R_i^2 D\,(C_\infty - C_s)\left(\frac{1}{R_i} + \frac{1}{\sqrt{\pi D t}}\right) - \\ - \frac{R_i^2 D}{2\sqrt{\pi}} \sum_{\substack{j=1 \\ j\neq i}}^{N} \int_0^t \frac{1}{R_i}\left(1 - \frac{R_i}{d_{ij}}\right) \frac{\dot{m}_j(t')}{[D(t-t')]^{3/2}}\, \exp\left(-\frac{(d_{ij}-R_i)^2}{4D(t-t')}\right) \mathrm{d}t'. \tag{3.10}$$

Note that the solution has been already extended to the case where N bubbles exist. This includes denoting by R_i the radius of the bubble under consideration and by d_{ij} its distance to the other bubbles in the cloud. To make the problem dimensionless we introduce the following dimensionless variables, $a = R/R_c$, $\Delta = d/R_c$, $\tau = Dt/R_c^2$ and $M = \dot{m}/(\rho_g D R_c)$, where R_c is a characteristic bubble diameter. Besides, the saturation level which indicates the amount of CO_2 available in the liquid is defined by $\zeta = C_0/Cs$ with C_0 the concentration in the liquid far away from the bubbles and C_s the saturation concentration at the ambient pressure P_s, that is $Cs = k_H P_s$. Let us introduce the Ostwald coefficient as $\Lambda = C_s/\rho_g$. With these definitions, equation (3.10) results

$$M_i = 4\pi a_i^2 \Lambda\,(\zeta - 1)\left(\frac{1}{a_i} + \frac{1}{\sqrt{\pi\tau}}\right) - \\ - \frac{a_i^2}{2\sqrt{\pi}} \sum_{\substack{j=1 \\ j\neq i}}^{N} \int_0^\tau \frac{1}{a_i}\left(1 - \frac{a_i}{\Delta_{ij}}\right) \frac{M_j(\tau')}{[\tau-\tau']^{3/2}}\, \exp\left(-\frac{(\Delta_{ij}-a_i)^2}{4(\tau-\tau')}\right) \mathrm{d}\tau'. \tag{3.11}$$

This mass flux must be completed with the mass conservation equation for the $i-$th bubble, namely

$$M_i = 4\pi a_i^2 \frac{\mathrm{d}a_i}{\mathrm{d}\tau}. \tag{3.12}$$

The changes in the volume of the bubble induce a velocity field which, sufficiently far away from its center, can be modelled as that of a volume point source. Thus, considering the whole cloud, each individual bubble moves as a result of the superposition of these flows. In the Stokes limit, the resulting bubble velocity can be computed using the solution provided by Michelin *et al.* (2018)

$$\bar{U}_i = \frac{1}{4\pi} \sum_{j\neq i}^{N} \frac{\bar{\mathrm{e}}_{\mathrm{ij}}}{\Delta_{ij}^2} \left(M_j - \sum_{j\neq l}^{N} \frac{a_j^3 M_l}{\Delta_{jl}^3} \left(1 - 3(\bar{\mathrm{e}}_{\mathrm{ji}} \cdot \bar{\mathrm{e}}_{\mathrm{jl}})^2\right)\right). \tag{3.13}$$

In this equation, $\bar{e}_{ij}$ is the unit vector joining the centers of the i-th and j-th bubble. In this work, we are going to let bubbles translate with only the first term of this formula since we expect $\left(a_j/\Delta_{jl}\right)^3 \ll 1$.

3.2.1 Numerical method

The computation of the time evolution of the bubble cloud is divided into two stages. First, we integrate equations (3.11) and (3.12) together assuming that the bubbles do not displace

and then, in a second stage, we compute the motion of the bubbles using the velocity field given by (3.13).

The system of integro-differential equations (3.11-3.12) is solved using an explicit Euler method for the temporal derivatives and a trapezoid method for the integral. Note that the kernel of the integral equation tends smoothly to zero at the integration limit $\tau' = \tau$, which makes unnecessary the usage of more sophisticated integration methods. We can distinguish two terms in equation (3.11), the first one corresponds to the mass flux provided by the Epstein–Plesset equation (Epstein & Plesset, 1950), which corresponds to the evolution of an isolated bubble. The second term, the integral, models the interaction between each individual bubble and the rest of the cloud. For the calculation of this second term we will adopt the simplificatory assumption that the radius of the bubble corresponds to the initial one (Frozen bubble). Note that this hypothesis is also adopted in the derivation of the Epstein–Plesset equation. The time step chosen for the simulations presented in this paper is $\Delta\tau = 10^{-3}$, which has been selected after verifying that making it smaller does not affect the results.

Once the time evolution of the bubble radii is computed, the bubbles are displaced with the velocity field given by (3.13) using also, for consistency with the previous stage, an Euler method with the same time step.

The start-up of the numerical computation is done by integrating solely the Epstein–Plesset equation up to the time step used for the rest of the calculation, $\Delta\tau$. Note that this is possible, since at very short times the concentration boundary layer is confined to a thin shell around the bubble of thickness $\sim \sqrt{\tau}$, which is much smaller than the typical bubble-bubble distance. This makes it possible to neglect the integral term in this first step.

3.3 Results and discussion

In this section we analyze the evolution of the size of the bubble clouds observed in our microgravity experiments, comparing it with that predicted by the model. As was explained above in §3.1, several key features of the bubble cloud, such as the number of bubbles or the initial size and spatial distributions cannot be determined experimentally. For this reason, the comparison will be of qualitative nature. Nonetheless, we will show that the model describes successfully the different regimes and behaviors observed experimentally.

Since the number of dimensionless parameters of the problem is large, we restrict our numerical results to initially spherical bubble clouds with a number of bubbles large enough to exhibit collective effects, namely $N = 100$, but evolving in liquids with different saturation levels, ζ. Furthermore, all the bubbles have the same initial size, $R_0 = 30$ μm. This radius is consistent with the estimated size of the bubble fragments that result in a similar cavitation experiment (Rodríguez-Rodríguez *et al.*, 2014). The initial positions of the bubbles are chosen randomly within a sphere, the cloud, of radius R_{bc}. To clearly identify the moment when bubbles start to interact with each other, it is convenient to seed the bubbles in the cloud with an average inter-bubble distance larger than one but still of order unity. Assuming that the volume of cloud available per bubble is $V_\mathrm{b} \sim \pi d^3/6$, setting $R_{bc} \approx 10R_0$ yields $d \approx 4.3R_0$, which fulfills the criterion. In what follows, all the lengths are shown made dimensionless with R_0 and the times with R_0^2/D, as done in the previous section.

Figure 3.4 shows qualitatively the evolution of a bubble cloud with a saturation $\zeta = 2$. The top row is the initial state, $\tau = 0$, whereas the lower one corresponds to the cloud at a later time $\tau = 3.2$. The color indicates the initial distance from the bubble to the center of the

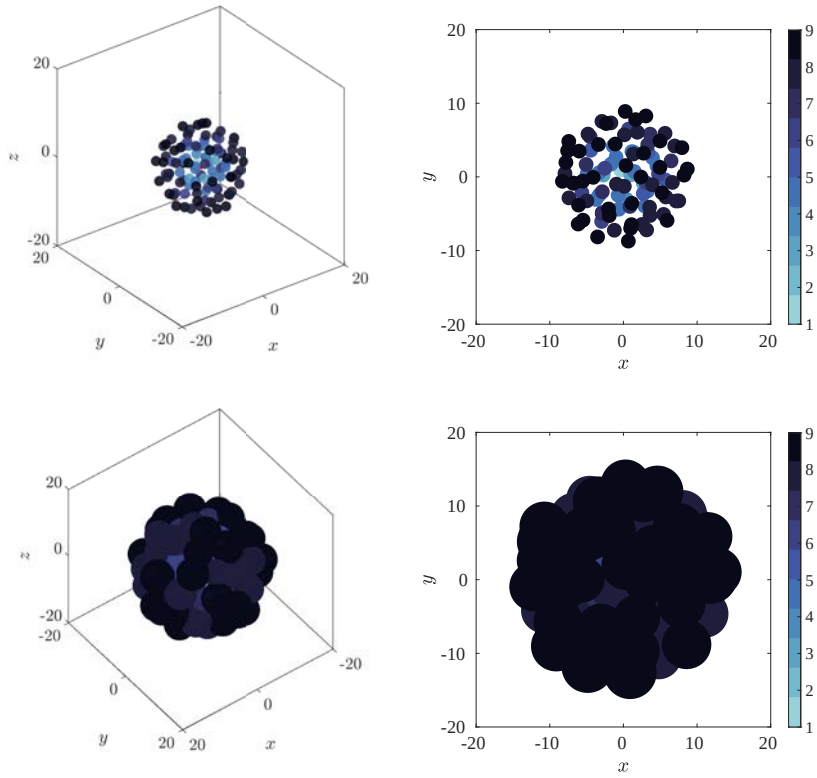

FIGURE 3.4. Three- and two-dimensional views of a bubble cloud at time $\tau = 0$ and at a later time, $\tau_{end} = 3.2$. The saturation of the liquid is $\zeta = 2$. The color represents the initial distance of each bubble to the center of cloud, growing from lighter to darker colors.

cloud, growing from light to dark hue. In fact, to present average results for bubbles located at a given distance from the center, the cloud radius has been divided into $B = 10$ layers equally spaced along the radius R_{bc}, with the color indicating the layer number. Using this averaging strategy we can show how bubbles grow at different depths inside the cloud.

Panels (a, c, e) of figure 3.5 show the time evolution of the radii of the bubbles in three clouds with saturation levels $\zeta = 1.01, 2, 4$, averaged over each radial layer. Correspondingly, panels (b, d, f) show the average bubble radius of each layer at the end of the simulation ($\tau \approx 6.5$). At early stages all the bubbles grow freely, that is, as isolated bubbles. In this situation, their growth is well described by the Epstein–Plesset equation (Epstein & Plesset, 1950), corresponding to the red dashed line in the figure. Using our notation, this equation reads

$$\frac{\mathrm{d}a}{\mathrm{d}\tau} = \Lambda\,(\zeta - 1)\left(\frac{1}{a} + \frac{1}{\sqrt{\pi\tau}}\right). \tag{3.14}$$

The departure from the growth predicted by this equation is a consequence of the fact that the thickness of the diffusive boundary layer around the bubble grows as $\delta \sim \sqrt{\tau}$. Therefore, until times of order $\tau \sim (\Delta/2 - 1)^2$ the boundary layers of the different bubbles do not interact

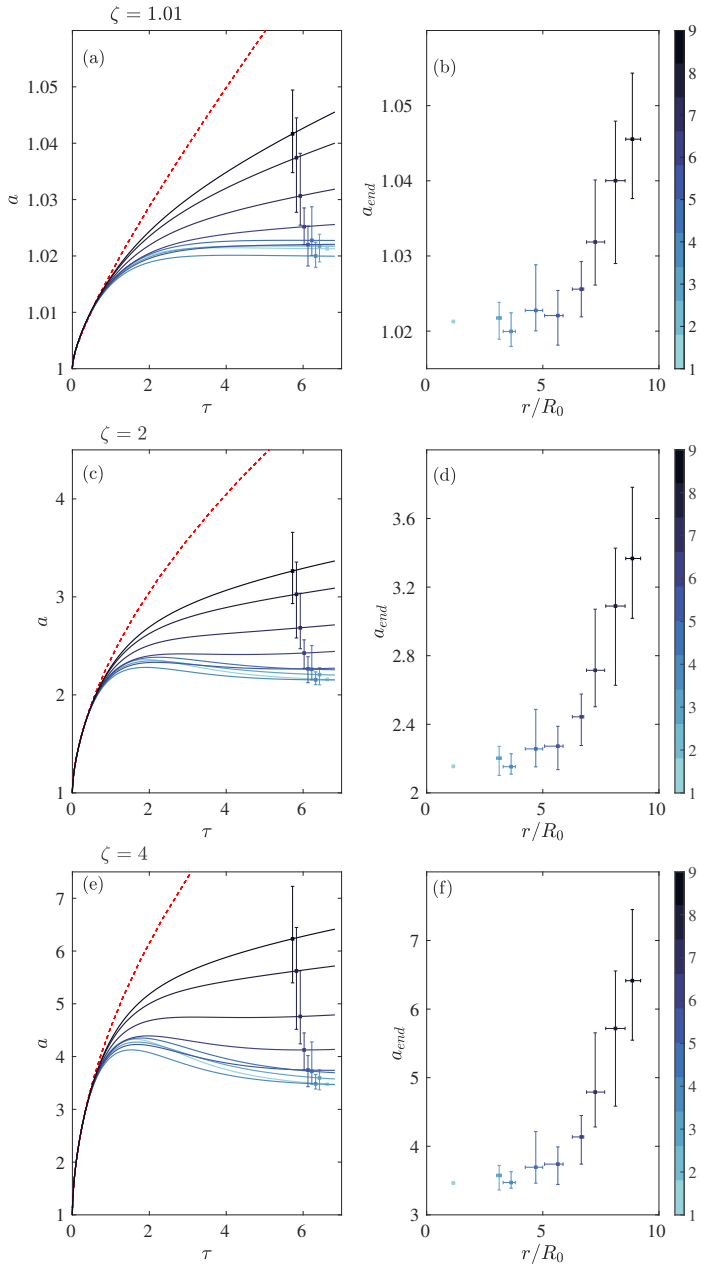

FIGURE 3.5. (a, c, e) Dimensionless time evolution of the bubble radii for saturation levels $\zeta = 1.01, 2$ and 4 respectively. The solid-line shows the mean radius for each cloud layer and the bars, the maximum and minimum radius of the bubbles for each layer respectively. The red-dashed line represents the growth of a isolated bubble predicted by Epstein–Plesset equation. (b, d, f) Final layer-averaged radius of the bubbles in the cloud as a function of its distance to the center. Markers represent the mean final radius, whereas the vertical bars show the maximum and minimum value of the radius and the horizontal bars the radial extension of each layer.

and bubbles do not feel each other. However, from that time on the diffusive boundary layers overlap and bubbles compete for the available CO_2. As a consequence, their growth rates diminish quickly, even becoming zero or slightly negative for bubbles in the innermost layers, where the access to the CO_2 present in the bulk outside the cloud is limited. Contrarily, the growth of the bubbles in the husk of the cloud goes on for large times, albeit at a much smaller pace. Note that the freezing of the growth of the innermost bubbles is consistent with the experimental observations (see figure 3.2 and the associated discussion). Regarding the slight reduction of the bubble sizes for deep bubbles observed in figure 3.5, although it seems analogous to Ostwald-rippening (Schmelzer & Schweitzer, 1987), surface tension is not considered here and thus this bubble size reduction is solely due to the intense absorption of CO_2 from the outermost bubbles.

The frozen radius of bubbles belonging to the innermost layers can be estimated using simple mass conservation arguments. Since these bubbles lose access to the CO_2 from the bulk liquid, they stop growing when they have absorbed all the excess CO_2 dissolved in the liquid volume of cloud available per bubble, which we can regard as that of a sphere of diameter d. Thus, the final mass, $4\pi/3\, R_f^2 \rho_g$, must the the sum of the initial one, $4\pi/3\, R_0^2 \rho_g$, plus the excess mass of CO_2 dissolved in the liquid volume with respect to the saturation one, namely $(C_\infty - C_S)\pi/6\, d^3$. In dimensionless terms this yields for the frozen radius

$$a_f = \left(1 + \Lambda\,(\zeta - 1)\,\Delta^3/8\right)^{1/3}. \tag{3.15}$$

For the saturation levels corresponding to the simulations in figure 3.5, with $\zeta = 1.01, 2$ and 4, the values of $a_f = 1.03, 2.22$ and 3.14 respectively. As can be observed in figures 3.5*b*, *d* and *f*, the agreement with the numerical results is fairly reasonable, given the assumptions adopted in this estimation.

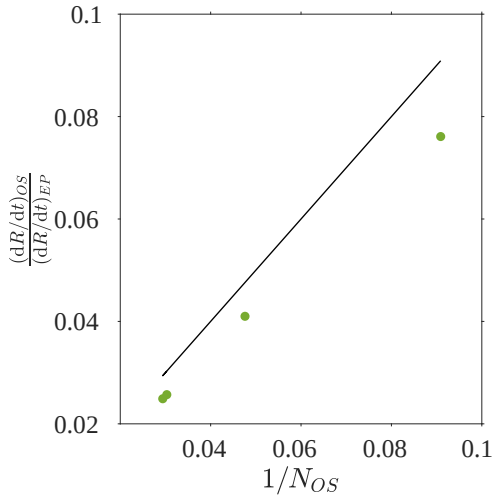

FIGURE 3.6. Rate of change of the radius of the bubbles in the outermost layer divided by that predicted by the Epstein–Plesset equation, as a function of the inverse of the number of bubbles in this layer. The solid line is $1/N_{os}$.

Once bubbles deep into the cloud reach this maximum size, it seems reasonable to assume that the bubbles in the outer shell are the only ones that continue growing. Because there

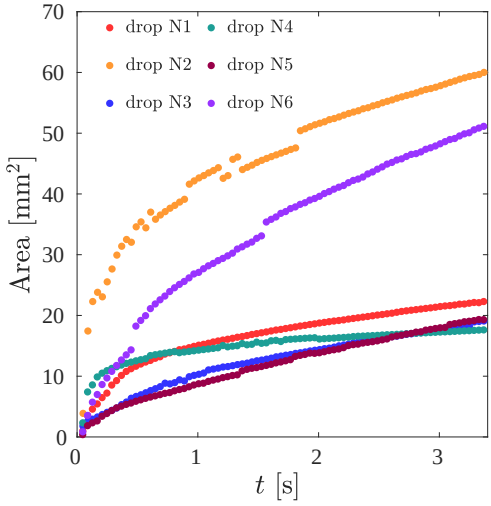

FIGURE 3.7. Evolution of the measured projected area of six bubble clouds. The level of saturation of the water in these experiments varies between 3.5 – 4.3.

is almost no CO_2 inside the cloud, all the mass flux comes across the outer boundary of the cloud. Moreover, this mass flux must be shared between all the bubbles in the outer shell. In a first approximation, we can model this effect by assuming that each bubble does no longer intakes gas from a solid angle 4π (that is, from all directions) but from a solid angle $4\pi/N_{os}$, where N_{os} is the number of bubbles in the outer shell. This means that the Epstein–Plesset equation can still be used to model bubble growth in the husk, but dividing its right hand side by the number of bubbles in the outer shell. To check this hypothesis, we plot in figure 3.6 the time derivative of the radius of the bubbles in the outermost layer at the end of the simulation divided by the one predicted by the Epstein–Plesset equation as a function of the inverse of the number of bubbles in this layer. These results correspond to the same saturation level, $\zeta = 2$, but to four different realizations. Because in each realization the bubbles are distributed randomly, the number of them in the outermost layer varies. The average value of this number can be estimated by assuming that the bubble density in the cloud is constant and that the outermost layer has a thickness of about $d/2$. Using simple geometrical analysis this yields $N_{os} \approx 3Nd/2R_{bc}$.

Although the radius of the individual bubbles cannot be determined experimentally, it is possible to measure the time evolution of the projected area of the whole cloud by applying image processing to each frame of the high-speed movies. The results for the six experiments conducted are show in figure 3.7. To compare these results against the simulations, we need to compute the time evolution of the projected area of the simulated cloud. To that end, we create synthetic images projecting the three-dimensional bubble cloud onto a plane, as done in figure 3.4. Using this technique, we easily take into account the effect of bubbles overlapping on the projected cloud area.

The physics behind the growth of the bubble cloud becomes more clear if we focus on the time derivative of the projected area rather than on the area itself. Figure 3.8 shows in logarithmic scale the rate of change of the area of the cloud for one of the views and for the six drops carried out in the campaign (see supplemental material for details on how the time

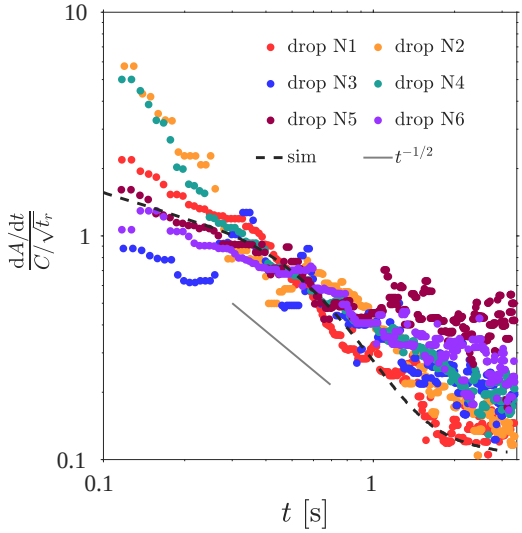

FIGURE 3.8. Rate of change of the projected area for the six drops, compared with that predicted by a simulation with $\zeta = 2$. The curves have been scaled with their corresponding value at the center of the time range where they follow the scaling law $dA/dt = Ct^{-1/2}$, that is $t_r = 0.4$ s. Here, C is the fitting constant of each experiment.

derivative of the area is calculated). The curves in the figure have been scaled with their value at the center of the time range where they obey the law $dA/dt \sim t^{-1/2}$ to be able to compare the evolution of clouds with very different initial sizes and thus growth rates. We plot also the rate of change of the area computed from a numerical simulation with $\zeta = 2$.

The model predicts the existence of three different stages in the evolution of the cloud which, despite their noise and variability, are also observed in the experiments. At short times, the area grows relatively fast, at a nearly constant rate. Later on, the rate of change of the area decays slightly faster than the square root of the time. Finally, at long times, the area grows again at a constant rate, albeit at a much slower pace.

The last two regimes can be easily explained with a simple heuristic model. Let us assume that the volume of the cloud is the sum of that of the N bubbles plus their associated water volume (a sphere of radius $d/2$). Since the water volume in the cloud does not change, the radius of such a cloud would then be

$$a_{bc} = N^{1/3}\left((d/2)^3 + a^3\right)^{1/3}. \tag{3.16}$$

The projected area, $A_{bc} = \pi a_{bc}^2$, has a rate of change

$$\frac{dA_{bc}}{d\tau} = 2\pi N^{2/3}\frac{a^2\dot{a}}{\left((d/2)^3 + a^3\right)^{1/3}}. \tag{3.17}$$

At short times, the radius of the bubble does not differ much from its initial one, $a \approx 1$, whereas its time derivative goes as $\dot{a} \sim t^{-1/2}$, as predicted by the Epstein–Plesset equation. Introducing this into Equation (3.17), we get $dA_{bc}/d\tau \sim t^{-1/2}$. This is in fairly good agreement with the

behavior observed at intermediate times in both experiments and theory. Actually, the rate of change of the area seems to decay slightly faster than this prediction, which is consistent with the fact that bubbles progressively stop growing, sooner the deeper they are in the cloud. In other words, the effective value of N in Equation (3.17) also decays with time, until it only refers to those bubbles located in an outer shell of thickness of order Δ.

At long times, the radius of the bubbles still grows as $a \sim t^{1/2}$, albeit with a prefactor smaller than that predicted by Epstein–Plesset, as discussed above. Moreover, $a \gg d/2$. In this limit, Equation (3.17) yields $\mathrm{d}A_{bc}/\mathrm{d}\tau \sim a\dot{a}$, which is constant. This is indeed what is observed to occur in the simulations and is qualitatively consistent with the experiments as well, despite the noise.

At short times, the model predicts a fast growth rate, not only in absolute value, which is to be expected as a consequence of bubbles obeying the Epstein–Plesset equation, but also in terms of how slowly it decays. Indeed, although Equation (3.17) suggests that $\mathrm{d}A_{bc}/\mathrm{d}\tau \sim \tau^{-1/2}$ at short times as well, this equation just takes into account the expansion of the boundaries of the cloud. However, during the first instants of the cloud evolution, the void fraction grows quickly. As a consequence, not only the cloud size grows as $\tau^{1/2}$, but bubbles inside also occupy increasingly larger areas of the projected cloud image, which explains the growth rate substantially faster than the square root of the time. Naturally, if we compute the total gas volume inside the cloud, V, we observe a much close agreement with $\mathrm{d}V^{2/3}/\mathrm{d}t \sim t^{-1/2}$, since bubble overlap does not affect its evolution. This can be observed in figure 3.9, where the evolution of the time derivative of $V^{2/3}$ is compared with that of the projected area of the cloud A for simulations with identical initial bubble distributions but different saturation levels.

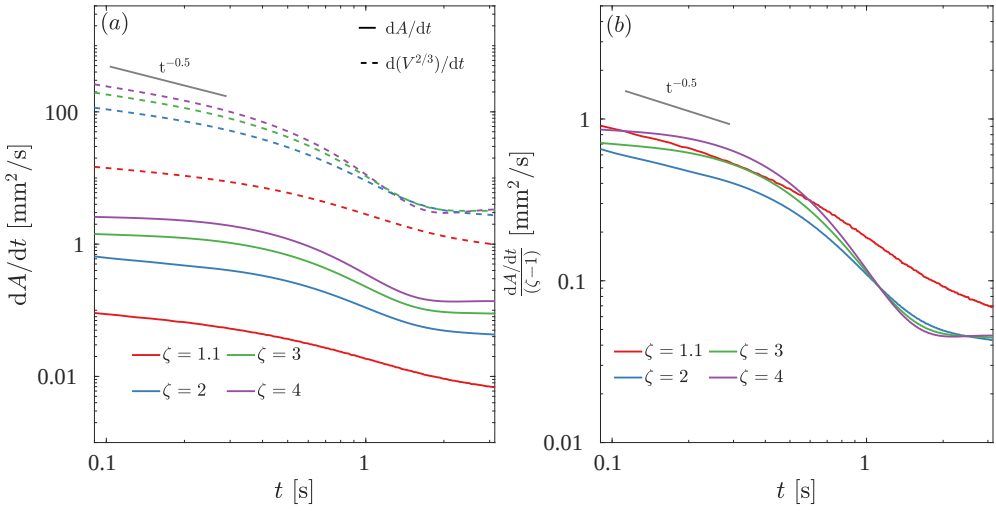

FIGURE 3.9. (a)Time derivative of the projected area and the volume raised to 2/3 for bubble clouds with identical initial configurations but different saturation levels, ζ.(b) Time derivative of the projected area divided by $(\zeta - 1)$.

In the experiments, the behavior at short times exhibits a larger variability. In some experiments we observe the trend $\mathrm{d}A/\mathrm{d}t \sim t^{-1/2}$ from the first instants, whereas in others the projected area shows a constant growth rate. We attribute this anomalous behavior to the fact that, at such short times, some of the clouds still keep some residual velocity as a result of the

implosion of the cavitation bubble which gave them birth. As this initial velocity dissipates, the projected area transitions to the regime where it decays as the inverse of the square root of the time. This residual velocity can be observed in the high-speed movies.

We conclude this section with a comment about the effect of the saturation level on the growth rate of the cloud. Unfortunately, the limited number of experiments that could be carried out in the drop tower and the lack of accuracy in the measurement of the saturation level, preclude us from exploring the effect of this parameter experimentally. However, we can still use our model to predict its influence on the results. Figure 3.9*a* shows how, for $\zeta \geq 2$, the evolution of both the projected area and the total gas volume is qualitatively independent of this value, just affecting the absolute value of the growth rates. Indeed, examination of the Epstein–Plesset equation (3.14) suggests that, provided the radius of the bubble is sufficiently larger than the initial one, the time derivative of the bubble radius scales with $(\zeta - 1)$. Because the mass flow rates are proportional to $\dot{a}$ and so are the bubble velocities, it is thus expected that the rate at which the cloud grows at any instant is proportional to this quantity. To check this hypothesis, we plot in Figure 3.9*b* the time derivative of the projected area divided by the supersaturation level, $\zeta - 1$. As predicted, the curves collapse fairly well at intermediate and long times. At short times, because the bubble radii are still close to the initial ones, the collapse is not so good. Consistently with this, the curve corresponding to the smallest saturation level, $\zeta = 1.1$, does not exhibit such a good collapse at any time, since the influence of the initial bubble radius last longer due to the smaller growth rates.

Acknowledgements

This work was supported by the Netherlands Center fro Multiscale Catalist Energy Conversion (MCEC), an NWO Gravitation programme funded by the Ministtry of Education, Culture and Science of the goverment of the Netherlands and the Spanish Ministry of Economy and Competitiveness though grants DPI2014-59292-C3-1-P and DPI2015-71901-REDT, partly funded through European Funds. I thank the team from the ZARM Drop Tower Operation and Service Company (ZarM FAB mbH) for valuable technical support during the experimental campaigns. The technicians, Manolo, David and Israel, from Universidad Carlos III for their technical labor in the experimental set up. The European Space Agency (ESA) for providing access to the drop tower through grants HSO/US/2015-29/AO and HRE/RS-PS/2018-7/AO.

3.A Extended experimental results

We present the post-processing analysis carried out for the high-speed movies obtained for the six drops. Regarding the image analysis, the projected area of the cloud have been tracked using custom-made image processing software implemented in Matlab. We started tracking this area from 2 or 3 frames after the spark generates the bubble cloud untill the end of the experiment. Thus, the time which the area is measured goes from 0.05 to 3.2 s.

As we said in §3.3, it is easier to observe the physics behind these experiments if we represent the time derivative of the projected area. To calculate the time derivative of the cloud size we use a central finite difference with a 4^{th} order of accuracy with a uniform grid spacing, $\Delta t = 0.001$s, despite of our time experimental resolution is 5e-4 s, to avoid the numerical noise. Then, we screen the data using a ten-point centered moving mean filter in order to see the growth trends. Figure 3.10a–f shows the evolution of the projected area (first column) and the filtered time derivative of the two perpendicular views for the six drops.

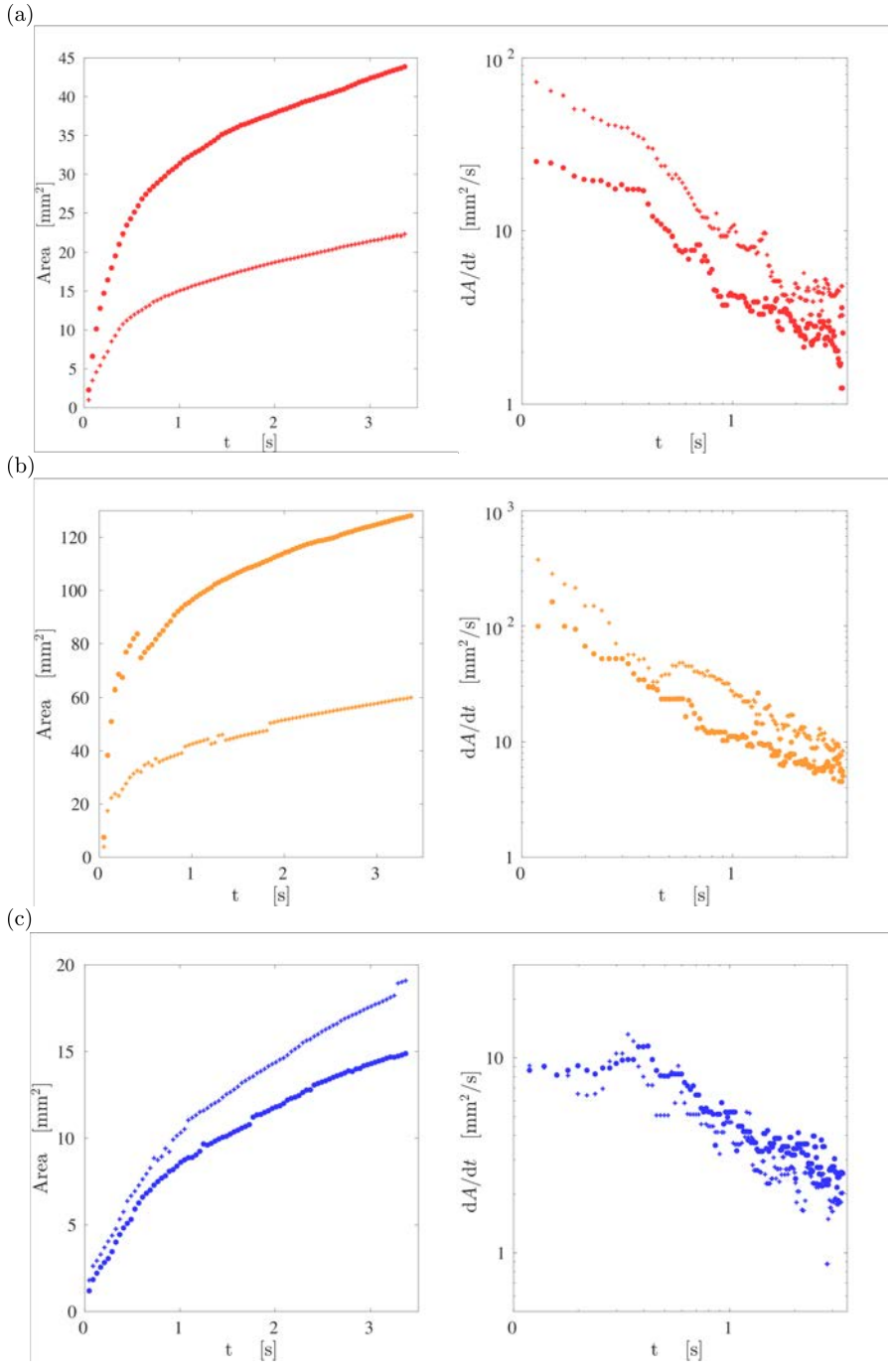

FIGURE 3.10. Continue in the next page.

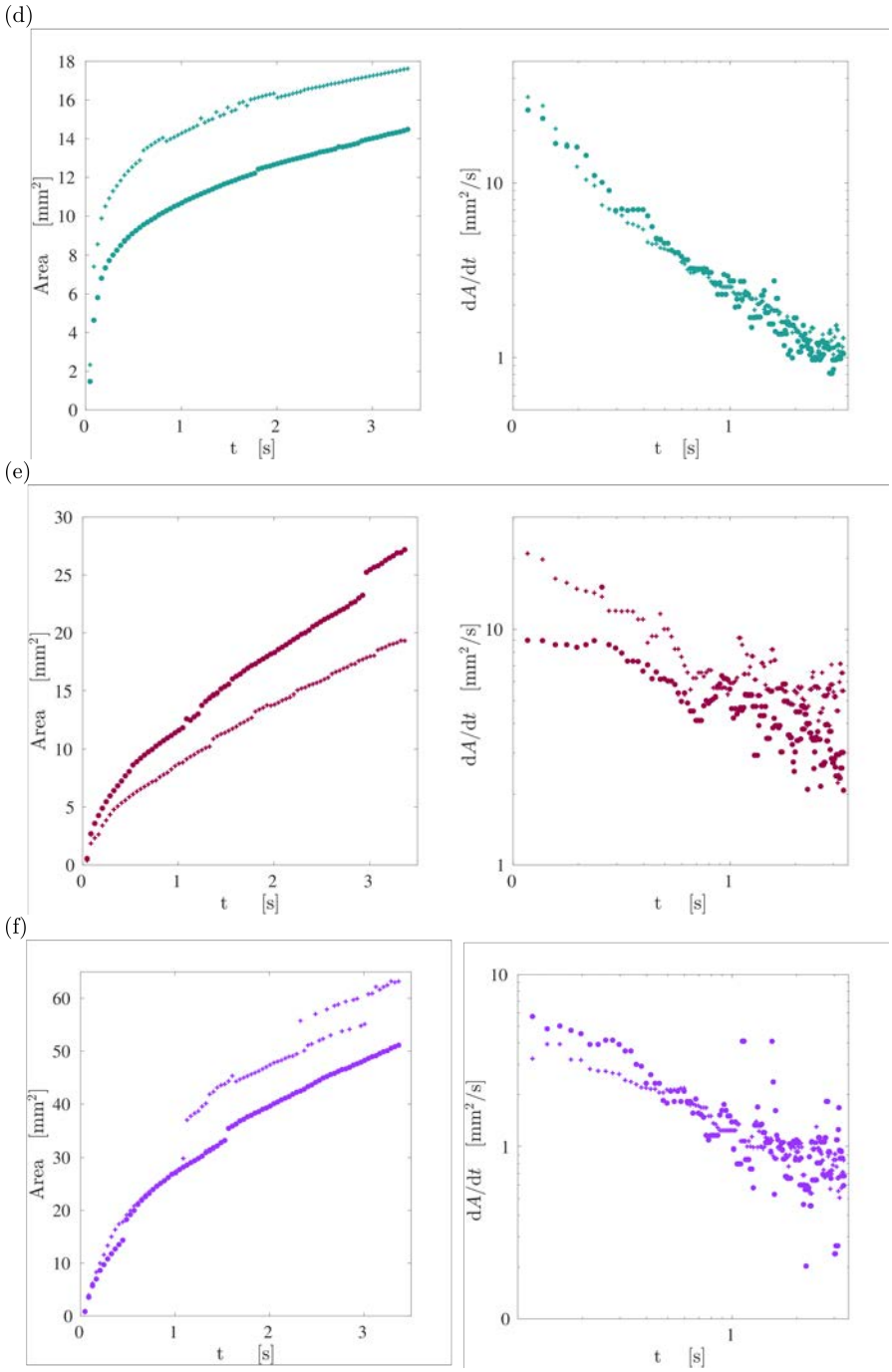

FIGURE 3.10. Projected area and the derivative of the projected area for the six drops from two perpendicular views.

CHAPTER 4

Conclusions

We designed, built, improved and tested an experimental set-up to explore the diffusion-driven growth of a bubble cloud in supersaturated liquids in microgravity conditions making used the drop tower facility in the German Center of Applied Space Technology and Microgravity (ZARM). The absence of gravity allows us to observe the purely diffusive growth dynamics of the bubble for several seconds, more than an order of magnitude longer than what could be observed under normal gravity (Rodríguez-Rodríguez *et al.*, 2014). Moreover, we avoid other effects such as natural convection (Enríquez *et al.*, 2014; Soto *et al.*, 2019).

In our preliminary results obtained in the first campaign, the evolution of the cloud can be observed for more than 1 second (Figure 2.5). Still, the cloud moves in the microgravity tests as a consequence of the residual velocity resulting from the implosion. Nonetheless, although the typical Peclet number, $Pe = VR_0/D$, computed with the measured bubble velocity, V, for the bubbles tracked in this study is relatively large ($Pe \approx 60$), the linear relation observed between the square of the bubble radii, R^2 and the time t suggests that advection plays a small role in bubble growth. This is consistent with the fact that, although the bubble cloud may translate as a whole, the relative velocity between each bubble and the fluid in its vicinity is much smaller than V. Consequently, we can apply the Epstein-Plesset equation (Epstein & Plesset, 1950) to predict bubble growth. Interestingly, the different slopes of the R^2 vs. t curves allow us to estimate the local concentration of CO_2 that every bubble experiences, which can later be connected to its location inside the cloud thanks to the 3D-reconstruction. Furthermore, the analysis of the grey level can be used to estimate quantitatively the time evolution of the total volume of gas in the cloud. This has been checked by calibrating the mean grey level using images where the gas volume was generated by electrolysis, so the latter could be accurately determined at all times.

In the second campaign, we improved the experimental set-up to solve the issues detected in the fist one, and explore the behavior of a dense bubble cloud close and the collective effects between bubbles. Although this way of producing the clouds introduces some variability in the experiments, the evolution of the six bubble clouds studied is qualitatively identical, which suggests that the diffusive growth mechanism that we study is fairly independent of the particular size or shape of the cloud.

Besides, inspired in these experimental observations, we have developed a mathematical model where each bubble grows competing for the available CO_2 with the others in the cloud, which are treated as point mass sinks. Although, strictly speaking, the model is only

valid in the limit of dilute bubble cloud, it predicts reasonably well the qualitative evolution observed in experiments. The good agreement of the model with the observations has allowed us to explain, using simple heuristic arguments, the experimental observations. Moreover, this model has been used to investigate aspects that could not be determined experimentally, namely the final distribution of bubble sizes inside the cloud and the effect of the saturation level.

References

References

Barrett, D. G. T., Kelly, S., Daly, E. J., Dolan, M. J., Drenckhan, W., Weaire, D. & Hutzler, S. 2008 Taking plateau into microgravity: The formation of an eightfold vertex in a system of soap films. *Microgravity Sci. Tech.* **20**, 17–22.

Brennen, C.E. 1995 *Cavitation and Bubble Dynamics.*. New York: Oxford University Press.

Cox, S. J. & G.Verbist 2003 Liquid flow in foams under microgravity. *Microgravity Sci. Tech.* **14**, 45–52.

Dyett, B., Kiyama, A., Rump, M., Tagawa, Y., Lohse, D. & Zhang, X. 2018 Growth dynamics of surface nanodroplets during solvent exchange at varying flow rates. *Soft Matter* **14**, 5197–.

Ehl, R.G. & Ihde, A. 1954 Faraday's electrochemical laws and the determination of equivalent weights. *J. Chem. Edu.* **31**, 226–232.

Enríquez, O. R. 2015 Growing bubbles and freezing drops: depletion effects and tip singularities .

Enríquez, Oscar R, Hummelink, Christian, Bruggert, Gert-Wim, Lohse, Detlef, Prosperetti, Andrea, van der Meer, Devaraj & Sun, Chao 2013 Growing bubbles in a slightly supersaturated liquid solution. *Review of scientific instruments* **84** (6), 065111.

Enríquez, O. R., Sun, C., Lohse, D., Prosperetti, A. & van der Meer, D. 2014 The quasi-static growth of co2 bubbles. *Journal of Fluid Mechanics* **741**, R1.

Epstein, P. S. & Plesset, M. S. 1950 On the stability of gass bubbles in liquid-gas solutions. *J. Chem. Phys.* **18**, 1505–1509.

FABmbH, ZARM & Fallturm, Am 2008 Zarm drop tower bremen user manual. *ZARM FABmbH University of Bremen, Bremen* .

FABmbH, ZARM & Fallturm, Am 2010 Zarm drop tower bremen general information. *ZARM FABmbH University of Bremen, Bremen* **28**.

Goh, B.H.T., Oh, Y.D.A., Klaseboer, E., Ohl, S.W. & Khoo, B.C. 2013 A low-voltage spark-discharge method for generation of consistent oscillating bubbles. *Rev. Sci. Instr.* **84**, 014705.

Gonnermann, H. M. & Manga, M. 2007 The fluid mechanics inside a volcano. *Annu. Rev. Fluid Mech.* **39**, 321–356.

Gramiak, Raymond & Shah, Pravin M 1968 Echocardiography of the aortic root. *Investigative radiology* **3** (5), 356–366.

Harrison, K. & Levene, J. I. 2008 *Electrolysis of water. Solar Hydrogen Generation.*. New York: Springer.

Homan, T., Gjaltema, C. & van der Meer, D. 2014 Collapsing granular beds: The role of interstitial air. *Phys. Rev. E.* **89**, 052204.

Jolliff, B. L. & Robinson, M. S. 2019 The scientific legacy of the Apollo program. *Physics Today* **72** (7), 44–50.

Koursari, N., Arjmandi-Tash, O., Trybala, A. & Starov, V. M. 2019 Drying of foam under microgravity conditions. *Microgravity Science and Technology* .

Liger-Belair, Gerard, Parmentier, Maryline & Jeandet, Philippe 2006 Modeling the kinetics of bubble nucleation in champagne and carbonated beverages. *The Journal of Physical Chemistry B* **110** (42), 21145–21151.

Medina-Palomo, A. 2015 Experimental and analytical study of the interaction between short acoustic pulses and small clouds of microbubbles. PhD thesis, Universidad Carlos III de Madrid.

Michelin, S., Guérin, E. & Lauga, E. 2018 Collective dissolution of microbubbles. *Phys. Rev. Fluids* **3**, 043601.

Obreschkow, D., Tinguely, M., Dorsaz, N., Kobel, P., de Bosset, A. & Farhat, M. 2011 Universal scaling law for jets of collapsing bubbles. *Phys. Rev. Lett.* **107**, 204501.

Peng, S., Spandan, V., Verzicco, R., Lohse, D. & Zhang, X. 2018 Growth dynamics of microbubbles on microcavity arrays by solvent exchange: experiments and numerical simulations. *J. Colloid Interf. Sci.* **532**, 103–111.

Rodríguez-Rodríguez, Javier, Casado-Chacón, Almudena & Fuster, Daniel 2014 Physics of beer tapping. *Physical review letters* **113** (21), 214501.

Saint-Jalmes, A., Marze, S., Safouane, M. & Langevin, D. 2006 Foam experiments in parabolic flights: Development of an iss facility and capillary drainage experiments. *Microgravity Sci. Tech.* **18**, 22–30.

Schmelzer, J & Schweitzer, F 1987 Ostwald ripening of bubbles in liquid-gas solutions. *J. Non-Equilibrium Thermodynamics* **12** (3), 255–270.

Soto, A. Moreno, Enríquez, O.R., Prosperetti, A., Lohse, D. & van der Meer, D. 2019 Transition to convection in single bubble diffusive growth. *Journal of Fluid Mechanics* **871**, 332–349.

Strong, F. C. 1961 Faraday's laws in one equation. *J. Chem. Edu.* **38**, 98.

Stuart, FM, Harrop, PJ, Knott, S & Turner, G 1999 Laser extraction of helium isotopes from antarctic micrometeorites: Source of he and implications for the flux of extraterrestrial 3he to earth. *Geochimica et Cosmochimica Acta* **63** (17), 2653–2665.

Vega-Martínez, Patricia, Rodríguez-Rodríguez, Javier, van der Meer, Devaraj & Sperl, Matthias 2017 Drop tower setup to study the diffusion-driven growth of a foam ball in supersaturated liquids in microgravity conditions. *Microgravity science and technology* **29** (4), 297–304.

Willert, C., Stasicki, B., Klinner, J. & Moessner, S. 2010 Pulsed operation of high-power light-emitting diodes for imaging flowvelocimetry. *Meas. Sci. Technol.* **21**, 075402.

Woods, Andrew W 2010 Turbulent plumes in nature. *Annual Review of Fluid Mechanics* **42**, 391–412.

Wu, Sean F 2015 The helmholtz equation least-squares method. In *The Helmholtz Equation Least Squares Method*, pp. 27–62. Springer.

Zhang, Youxue & Kling, George W 2006 Dynamics of lake eruptions and possible ocean eruptions. *Annu. Rev. Earth Planet. Sci.* **34**, 293–324.

Zhu, X., Verzicco, R., Zhang, X. & Lohse, D. 2018 Diffusive interaction of multiple surface nanobubbles: shrinkage, growth, and coarsening. *Soft Matter* **14**, 2006–.

Part II

Fast lifting of a plate from a water surface

CHAPTER 5

Introduction

Marine and naval structures commonly experience impact loads caused either by waves or by the motion of the structure into and out of water. For instance, ship sections enter the water and then subsequently exit it in rough sea conditions, a process known as slamming. A related phenomenon, wetdeck slamming, is observed in offshore engineering, where a wave hits the wetdeck of a platform from below, a problem studied both experimentally and numerically by Baarholm (2001), Baarholm & Faltinsen (2004), Faltinsen *et al.* (2004), and Scolan *et al.* (2006). During a first stage, the wetted area of the deck increases in time leading to high hydrodynamic loads. Then, during the second stage, the wetted area diminishes as the wave propagates away from the platform.

It is common wisdom that a body that enters a water surface at high speed may experience very large forces. However, it is less obvious that forces of similar magnitude –but opposite sign– act in the opposite case, i.e. when the body exits water. Commonly, hydrodynamic loads are defined as positive during the entry stage, and negative during the exit one. Here, negative loads mean that the hydrodynamic pressure acting on the wetted part of the ship hull is below the atmospheric pressure, albeit still above the vapour pressure at which cavitation occurs. It is remarkable that, although the exit stage lasts longer than the entry one, the magnitude of the negative loads can be comparable to the magnitude of the positive ones (Faltinsen *et al.*, 2004; Scolan *et al.*, 2006; Piro & Maki, 2011). Despite these similarities, the physical origins of these loads are different. While the positive loads during the entry stage scale with the dynamic pressure and thus are proportional to the entry velocity of the body squared, negative loads during the exit stage are governed mainly by the acceleration, provided this is much larger than gravity. Conversely, if the body leaves the water slowly, then gravity and hydrostatic pressure play the major roles (Greenhow, 1988; Rajavaheinthan & Greenhow, 2015). Despite water entry being much related to water exit, the former problem has been studied extensively in the past (Korobkin & Pukhnachov, 1988), while the latter has received comparatively less attention.

We mention here several studies that emphasize the water exit stage. Two-dimensional problems of water entry and exit were investigated numerically by Piro & Maki (2011, 2012, 2013) using full Navier–Stokes simulations. In particular, they computed the impact of a rigid wedge with deadrise angle of 10°, initial velocity 4 m s^{-1} and a deceleration of 92 m s^{-2}. They found that the hydrodynamic force is initially positive and then becomes negative even though the wedge continues to penetrate the water. Later, the magnitude of the negative

hydrodynamic force reaches a maximum at the end of the entry stage, when the speed of the wedge is zero, and continues to be negative with a decreasing magnitude during the exit stage.

Recently, the development of analytical and semi-analytical approaches to calculate hydrodynamic loads in water-exit problems has become of interest. Korobkin (2013) developed a linearised model that was in excellent agreement with existing computational results (Piro & Maki, 2011). In this model, both the hydrodynamic equations and the boundary conditions were linearised by exploiting the fact that, at small times, displacements are small. In particular, this allows us to impose the boundary conditions on both the free surface and the surface of the moving body on the initial equilibrium level of the water. The actual shape of the body was not included in the model, and neither were gravity, surface tension and viscosity. The problem was then formulated for an acceleration potential, which is zero on the free surface. The wetted part of the body surface diminishes during water exit. The speed of the contact line, which bounds the wetted part of the body surface, is set to be proportional to the local velocity of the flow along the body surface. This condition was introduced by Baarholm & Faltinsen (2004) and Faltinsen *et al.* (2004) in a two-dimensional problem of wetdeck slamming with the coefficient of proportionality between fluid and contact line speeds, γ, being equal to one. This is, the contact line was assumed to be a material one. Korobkin (2013) set $\gamma = 2$ using the computational results by Piro & Maki (2011) regarding the hydrodynamic force during the exit stage. The linearised model of water exit with a constant deceleration provides hydrodynamic forces which are very close to those computed with the Navier–Stokes solver (see figure 5 for a wedge and figure 6 for a parabolic contour in Korobkin (2013)). The comparison becomes even better if nonlinear effects and gravity are included in the exit model by using the approximations suggested by Korobkin (2004) and Khabakhpasheva *et al.* (2016).

The linearised model of two-dimensional water exit was generalised, and validated using CFD results, by Korobkin *et al.* (2017*a*) to include arbitrary motions of bodies and bodies of time-varying shapes. The model was developed further to be included in the two-dimensions-plus-time analysis of aircraft ditching. Korobkin *et al.* (2017*b*) presented another model of water exit, which is based on a small-time asymptotic solution of the two-dimensional problem of a plate lifted suddenly from the water surface and on the method of matched asymptotic expansions. A similar model was developed by Iafrati & Korobkin (2008) for water impact problems. In this theoretical study of water exit the flow near the edges of the plate and the motion of the contact line are nonlinear and self-similar, in contrast to the flow in the main region, which is linear at leading order for small displacements of the plate. The acceleration of the contact line was found to be proportional to $t^{-\frac{2}{3}}$ for a constant acceleration of the plate lifting, where t is the time. Note that this result is valid also for the three-dimensional lifting problem of a floating plate with smooth edge, where the flow near the plate edge is two-dimensional at the leading order during the early stage of the motion, see Scolan & Korobkin (2003). The predicted shape of the free surface near the contact points was found to be very close to full Navier–Stokes numerical simulations. Note that, in the linearised exit model, the free-surface shape is very different from the computed one, despite the fact that the theoretical hydrodynamic forces compare well with experiments.

A simplified description of water entry and exit is provided by the von-Kármán model (Von Karman, 1929), which defines the wetted part of a body surface during both the entry and exit stages as the intersection of the body surface with the flow region determined without the effect of the body presence. This idea was used in water exit problems by Tassin *et al.* (2013) to estimate the hydrodynamic loads for bodies with time-dependent shapes. However

Faltinsen *et al.* (2004) pointed out that, using the von-Kármán approach, the calculated duration of the water-exit phase of a body is shorter than the experimentally observed one. Despite this discrepancy in the calculated duration of these stages, the peak values of the forces obtained with this method were still comparable in magnitude. In our problem, this model cannot be used because the flat disc, which has negligible draft, leaves the initial liquid region immediately after it starts to move upwards.

Due to the complexity of the exit flows with unsteady free surfaces, both numerical and theoretical findings and models should be validated against experiments. To the best of our knowledge there are few works that can be used to validate experimentally the kinematics of water-exit flows, but not the hydrodynamic loads, which are difficult to measure. Two papers are worth highlighting as they focus specifically on water-exit (Reis *et al.*, 2010; Tassin *et al.*, 2017). The seminal study by Reis *et al.* (2010) deals with the volume of water dragged by a lifting disc that mimics a cat's tongue. This disc was controlled by a computer to reproduce the observed motion of an actual tongue, in particular reaching accelerations as high as 27 m s^{-2}. The dragged water volume was determined using high-speed imaging. They concluded that the domestic cat laps exploiting "fluid inertia to defeat gravity and pull liquid into the mouth". Despite the interest of the experiment, these authors did not measure the forces required to pull the disc, so their results cannot be used to validate water exit theories (Korobkin, 2013; Korobkin *et al.*, 2014*a*). Tassin *et al.* (2017) reported experiments where they measured the dynamics of the contact line, or in other words the evolution of the wetted area. The acceleration of a circular transparent plate was measured to be between 0 and 25 m s^{-2}. Furthermore, they showed that the radius of the wetted region closely follows the radius predicted by the linearised exit model with $\gamma = 1$. Recently Tassin *et al.* (2018) published experimental results for both a circular disc and a cone lifted from the water surface. The radius of the disc was 20 cm and the deadrise angle of the cone was 15 degrees. Initially the water was at rest and the circular disc touched the water surface with negligible initial draft. The initial radius of the wetted surface of the cone varied from 10 to 25 cm. The disc and cone were lifted vertically by a hexapod which imposed a prescribed time-varying displacement with maximum speed 0.6 m/s and relatively small accelerations comparable to gravity. The maximum measured magnitudes of the suction forces were about 35 N with a duration of about 0.25 s. It was concluded that the measured hydrodynamic forces were in rather good agreement with the numerical results obtained with the ABAQUS/Explicit solver.

Some ideas about the hydrodynamic forces during water exit can be gained from experiments with a body moved by a given external force. Then the measured acceleration of the body motion can be used to determine the evolution of the hydrodynamic force acting on the body. This idea was employed by Korobkin *et al.* (2014*b*) who studied experimentally, numerically and theoretically the oscillations of a rigid sphere entering and exiting a water surface. The sphere was supported by a spring with the equilibrium position above the water surface. These experiments demonstrated that the hydrodynamic force was negligible in the conditions reported. Theoretical analyses revealed that, for these forces to be relevant, the added mass of the wetted sphere should be at least comparable to the body mass. Moreover, it was concluded that the hydrodynamic force would be more visible if the body moved at a higher acceleration. These conclusions follow from the linearised exit model, which states that the hydrodynamic force is proportional to both the added mass of the body and the body acceleration.

With the aim of quantifying experimentally the hydrodynamic loads during water exit, in this work we present an experimental investigation of the loads acting on a circular plate,

a disc, lifted impulsively from a water surface with a high acceleration. Initially the disc touches the flat water surface with a negligible draft. Then the disc is moved suddenly upwards by a given external force applied around its center. Both the pulling force and the disc acceleration are measured with high temporal resolution in order to resolve the initial few milliseconds of the motion, when the highest loads occur. Besides measuring force and acceleration, we use high-speed cameras to record the disc displacement and the radius of the wetted area. The disc acceleration peaks at about 200 m s^{-2} in our experiments and then rapidly decays despite the fact that the external force continues to increase. We also observe that the wetted area of the disc does not change before the disc acceleration peaks. This behaviour of the disc acceleration and its wetted area is attributed in this study to the interaction between the hydrodynamic loads and the elastic deflection of the disc. To explain and quantify theoretically these measurements, we introduce a model that solves the unsteady axisymmetric flow generated by a lifted elastic body coupled with its elastic deformations. This new model explains both the non-monotonic relation between the disc acceleration and the applied external force and the delay in the shrinking of the wetted part of the disc surface. The model is finally validated quantitatively by dedicated experiments with circular discs of different rigidities. Notice that these hydroelastic effects are not expected to be observed in the experiments by Tassin *et al.* (2018) because of the smooth lifting of the bodies, i.e. with small accelerations. Although, to the best of our knowledge, there are no models of water exit taking into account hydroelastic effects, a relevant axisymmetric problem of water entry of an elastic conical shell was studied theoretically by Scolan (2004). We use some techniques and the notation of this study to develop our model of hydroelastic water exit.

CHAPTER 6

Hydro-elastic effects during the fast lifting of a disc from a water surface [‡]

Here we report the results of an experimental study where we measure the hydrodynamic force acting on a plate which is lifted from a water surface, suddenly starting to move upwards with an acceleration much larger than gravity. Our work focuses on the early stage of the plate motion, when the hydrodynamic suction forces due to the liquid inertia are the most relevant ones. Besides the force, we measure as well the acceleration at the center of the plate and the time evolution of the wetted area. The results of this study show that, at very early stages, the hydrodynamic force can be estimated by a simple extension of the linear exit theory by Korobkin (2013), which incorporates an added mass to the body dynamics. However, at longer times, the measured acceleration decays even though the applied external force continues to increase. Moreover, high-speed recordings of the disc displacement and the radius of the wetted area reveal that the latter does not change before the disc acceleration reaches its maximum value. We show in this paper that these phenomena are caused by the elastic deflection of the disc during the initial transient stage of water exit. We present a linearised model of water exit that accounts for the elastic behaviour of the lifted body. The results obtained with this new model agree fairly well with the experimental results.

6.1 Experimental study of the water exit

Here, we present the facility designed to measure the hydrodynamic forces acting on an object suddenly lifted from a water surface at an acceleration much larger than gravity, $a \gg g$. Besides the force pulling the object and its acceleration, we also measure the evolution of the wetted area or, conversely, the recoil of the liquid-gas-solid contact line.

The layout of the experimental apparatus is shown in figure 6.1.

The plate is set in motion by a structure which operates as a catapult. A mobile arm, a seesaw, turns around a fulcrum located in a fixed structure anchored to the ground. The plate is supported by a steel bar that hangs from one end of the mobile arm through a steel cable. An

[‡]Experiments performance, analysis and comparisons by P.Vega-Martínez. Formulation of the problem and solution was developed by T. Khabakapasheva (section 6.3). All the authors discussed the ideas and results and wrote the article.

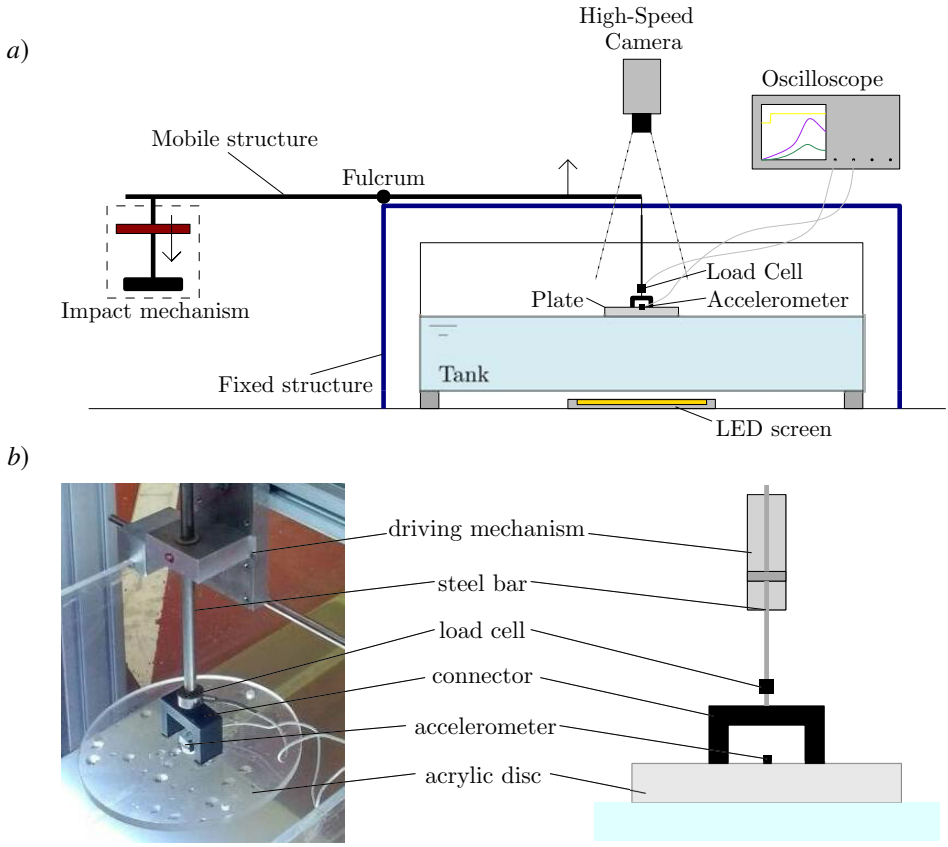

FIGURE 6.1. (*a*) Layout of the experiment. (*b*) Detail of the plate, which is connected to a driving mechanism through an inverted U-shape structure fixed at its upper surface.

Radius, R	10.8 cm
Thickness, h_p	1 cm
Mass of the plate, M_p	0.432 kg
Mass of the equipment, M_c	0.198 kg
Added mass of the plate, m_a	1.680 kg
Total mass, $M = M_p + M_c$	0.630 kg
Density, ρ_p	1180 kg m^{-3}
Young's modulus, E	3.1×10^9 Pa
Poisson ratio, ν	0.33

TABLE 6.1. Summary of the features and material properties of the plate.

auxiliary structure guides the movement of the steel bar, to guarantee that its motion is purely vertical. The other end of the arm is connected to the impact mechanism, which consists in a weight that slides along a rail and a base that stops its fall and thus transmits the impact to the seesaw.

The bar connects to the plate through a fast-speed-of-response load cell (Honeywell Model 31 mid, 100 lb), capable of measuring forces of up to 450 N. The disc is equipped with an accelerometer (Honeywell model JTF ± 50G), placed at its centre. The signals from the load cell and the accelerometer are read by an oscilloscope (Tektronik TDS3014c, sample rate of 250 kHz), after having been pre-conditioned by amplifiers (ADAM 3016). During postprocessing, the acceleration of gravity and the weight of the plate are subtracted from the results.

The plate, whose properties are summarised in table 6.1, is made of transparent acrylic to allow for the observation of the contact line motion. The total mass of the equipped disc, M, is the sum of the mass of the plate, M_p, the connector, accelerometer and load cell, M_c. The connector and the steel bar between the load cell and the driving mechanism are considered as perfectly rigid in the present analysis. They are made of aluminium, which is much stiffer than the material of the plate.

At the beginning of the experiment, the weight (5 kg) is released and allowed to fall freely (from a height of 10 cm), sliding down the rail until it impacts the base. When this happens, this instant is regarded as the time origin, $t = 0$.

We perform two kinds of experiments, one where the plate is touching the water surface of the tank (wet experiment), and another one, identical in everything to the first one, except in that the disc does not touch the water surface (dry experiment). Wet experiments are carried out with the disc touching the water surface of a tank, whose dimensions, 100 x 40 x 40 cm^3, are large enough to guarantee negligible boundary effects.

To illustrate the good repeatability of the results, we plot in figure 6.2 the acceleration and force corresponding to wet experiments performed under identical conditions (see table 6.2, session 3, for details). To make clear the point that the curves are essentially the same, within the experimental variability, they have been shifted a small time to compensate for the uncertainty in the determination of the impact time ($\Delta t_1 = 0.2$ ms, $\Delta t_2 = 0.7$ ms, $\Delta t_3 = -0.6$ ms and $\Delta t_4 = 0.85$ ms). The relative discrepancy in the peak scaled forces (figure 6.2a) is less than 8.3%, whereas that in the peak accelerations (figure 6.2b) is less than 7.2% for the four repetitions.

The motion of the contact line, in other words the evolution of the wetted area, is recorded

Session	Dry/Wet	M (kg)	h_p (cm)
1	Dry	0.630	1
2	Wet	0.630	1
3	Wet	0.630	1
4	Wet	1.070	2
5	Wet	0.430	0.5

TABLE 6.2. Summary of the experimental sessions. Sessions 2 and 3 are identical in their conditions, but high-speed movies were acquired only for session 3.

by a high-speed camera (NAC Memrecam HX-3) working at 15000 fps. To acquire clear top-view images, we use a LED light (Metaphase Technologies, 9" x 16" White, LED Backlight) at the bottom of the tank, so that the perimeter of the disc and the contact line are visible as black lines during the experiment. This lighting configuration is similar to the configuration denoted as "central LED lighting" in Tassin *et al.* (2017). Moreover, high-speed movies are taken from the side, to compare the evolution of the wetted radius with the distance the plate has risen. Examples of the images used to measure these quantities are shown in figure 6.3, along with a sketch of their definitions.

A few comments should be made here about the image processing techniques used to measure the time evolution of the wetted area. We track the contact line using a custom-made image processing software implemented in Matlab based on the so-called Hough transform (Yuen *et al.*, 1990). The Hough transform is a well-known technique used in image analysis to find objects with a given shape, in this case circles, by a voting procedure. In a first step we detect the edges of images like those in figure 6.3(e-h). In this way, two families of pixels are found near the region of interest where the contact line is expected to be found: pixels belonging to the edge of the disc and pixels belonging to the contact line. Each edge point detected adds one vote to all the possible circles that it can belong to. Repeating this procedure for all the edge points, we create a histogram in the parametric space of possible circles, whose local maxima correspond to the circles actually found in the image, i.e. containing a large number of points. In the case of the images shown here, this histogram exhibits two peaks, which correspond to the plate edge and the contact line respectively. We should point out that, using this procedure, it is possible to detect the contact line when it is still very close to the plate edge. Thus, this technique proves to be essential to capture the first instants of the contact line motion.

6.2 Comparison of the linearised theory of water exit with experiments

In this section we present the results of the experiments summarised in table 6.2. For each realization the accelerometer and load cell provide the acceleration of the center of the plate and the total force pulling it upwards, respectively. Moreover, the contact line dynamics and the height of the plate during the first instants are obtained through digital image processing of high-speed movies.

The accelerometer measures the acceleration of the plate, $a(t)$, whereas the load cell measures the total force, $F_{exp}(t)$, with which the driving mechanism pulls the instrumented plate of mass M. These quantities, together with the hydrodynamic force $F_h(t)$, are related

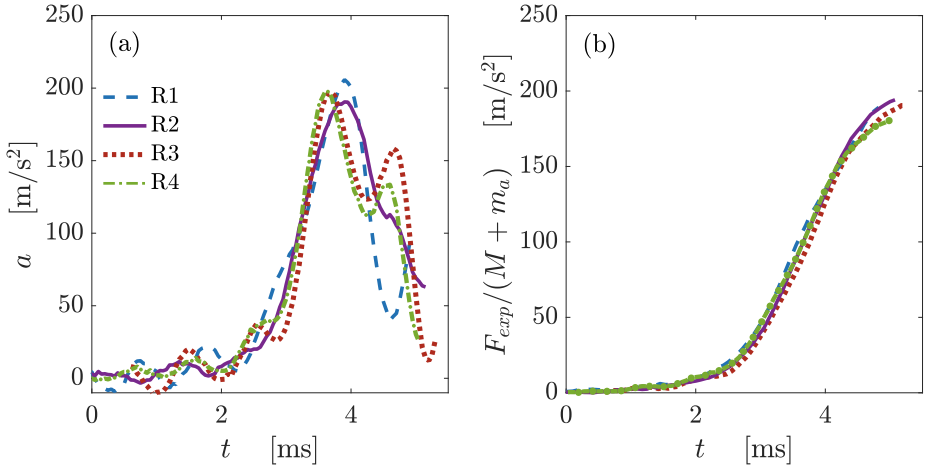

FIGURE 6.2. Comparison between acceleration and force measurements obtained under identical experimental conditions for four repetitions of session 3.

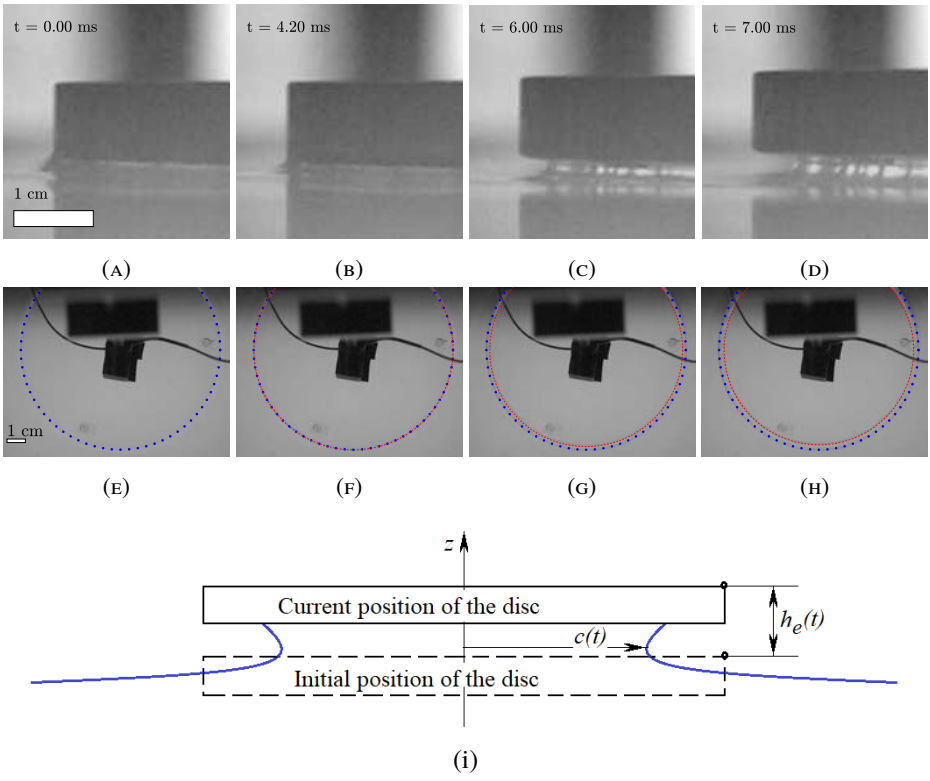

FIGURE 6.3. (a–d) Side view of the edge of the plate and (e–h) top view of the plate where the blue dots mark the diameter of the plate and the red dash traces the detection of the contact line. Images acquired at 15000 fps. (i) Definition of $c(t)$ and $h_e(t)$.

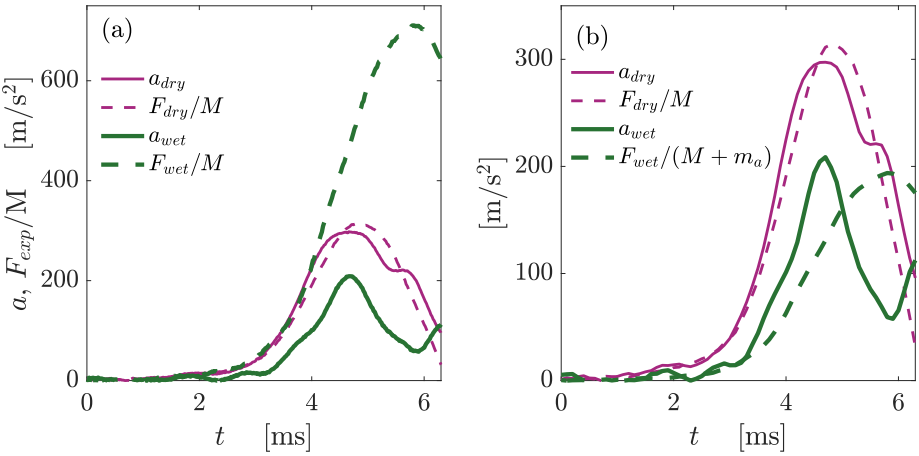

FIGURE 6.4. Comparison between the force and acceleration measurements obtained in a dry and a wet case respectively. Sessions 1 and 2 from table 6.2.

through Newton's second law:

$$F_{exp} = F_h + Ma. \tag{6.1}$$

From the linearised theory of Korobkin (2013), F_h is approximated by the product of the disc added mass, m_a, times the disc acceleration, a,

$$F_h = m_a\, a, \quad \text{where} \quad m_a = \frac{4}{3}\rho c^3, \tag{6.2}$$

thus F_{exp} is expected to be proportional to a,

$$F_{exp} = \left(M + \frac{4}{3}\rho c^3\right) a, \tag{6.3}$$

with c denoting the radius of the wetted area, see figure 6.3i. The added-mass term arises from the suction pressure forces that the plate communicates to the parcel of surrounding liquid that follows its accelerated motion. The effect of these forces is equivalent to endow the plate with an additional mass that must be also accelerated with it, thus effectively increasing its apparent inertia. Note that, in our experiments, this added mass is indeed much larger than the mass of the instrumented disc itself, see table 6.1.

To highlight the relevance of this hydrodynamic suction force, F_h, we show in figure 6.4a the force and acceleration measured for the same experimental conditions, but in two realizations with the plate being dry and wet respectively. While in the dry case, $F_h = 0$, the force divided by the mass of the plate coincides with the acceleration within the experimental variability, the acceleration in the wet case is substantially smaller, as a consequence of the hydrodynamic suction force that pulls the plate downwards. Figure 6.4b shows that, taking into account the added mass of the wetted plate, yields a reasonable agreement with equations (6.1) and (6.3) during the initial period of 3.5 ms only.

It should be pointed out that the radius of the wetted area, $c(t)$, as well as the forces and the plate's acceleration, are functions of time. However, in practice it is possible to neglect the recoil of the wetted area, since its radius, c, barely departs from that of the disc, R,

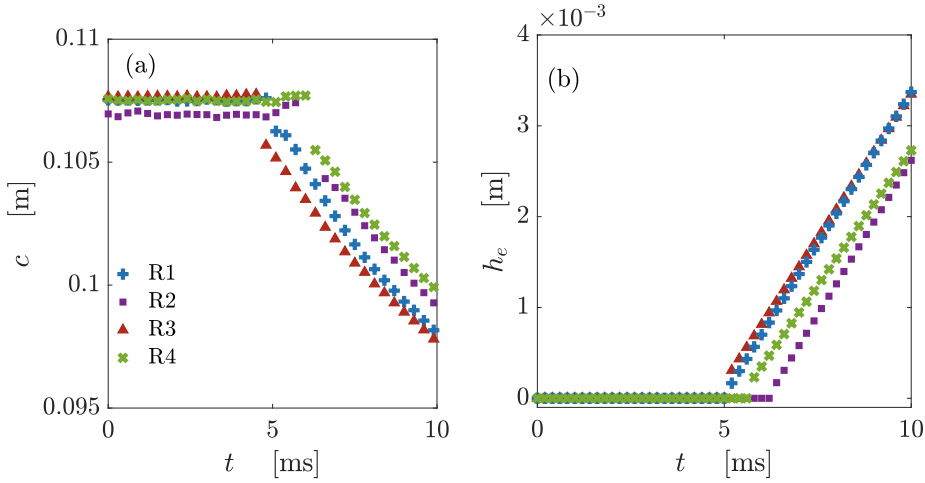

FIGURE 6.5. Evolution of the radius of the wetted area and the vertical displacement of the edge of the plate for four experimental realizations of session 3.

along the duration of the experiment, always shorter than 10 ms. This is supported by the measurements of the evolution of the wetted radius shown in figure 6.5. Figure 6.5a does not show any variation of the wetted area during the first 4 ms. Indeed, until the plate moves of the order of the capillary length (around 2 mm, see figure 6.5b) the contact line recoils a very small distance. In order to further prove this, we record movies of the side view of the experiment focusing on the edge (Figure 6.3a-d). Note that only after 4 ms the motion of the contact line can be determined from the top-view, when the contact line detaches from the edge and slides along the lower surface of the plate. In summary, these observations support that $c(t)$ can be approximated as R in the calculations of the hydrodynamic force.

At longer times, when the contact line detaches from the edge and recoils, its position can be related to the instantaneous displacement of the plate edge, $h_e(t)$, using the ideas of Korobkin *et al.* (2017). In that paper, the authors found a self-similar solution to describe the dynamics of the free surface close to the edge of a plate lifted from the water surface at a large constant acceleration. This solution predicts that the contact line displaces a distance $\Delta c = R - c \sim t^{4/3}$ with time. On the other hand, since the acceleration was assumed constant, then $h_e \sim t^2$. Combining these estimates, we get $\Delta c \sim h_e^{2/3}$. Even though the acceleration is not constant in our experiments, this power law seems to be recovered once the contact line starts to slide along the plate, as illustrated in figure 6.6. The data shown in this figure corresponds to early times, when the displacement of the contact line is smaller than about 10% of the plate radius. Thus, although the plate is circular, the dynamics of the contact line near the disc edge is approximately two-dimensional, and covered by the analysis of Korobkin *et al.* (2017).

Figure 6.4b sheds light on the dynamics of the coupled water-disc system. Although at short times the acceleration compares reasonably well with the prediction derived from equations (6.1) and (6.2), at about $t \approx 4.5$ ms the behavior of the acceleration changes dramatically. In particular it decays, which is in clear contradiction with these equations, which predict a linear relation between F_{exp} and a. They are not proportional any more, but

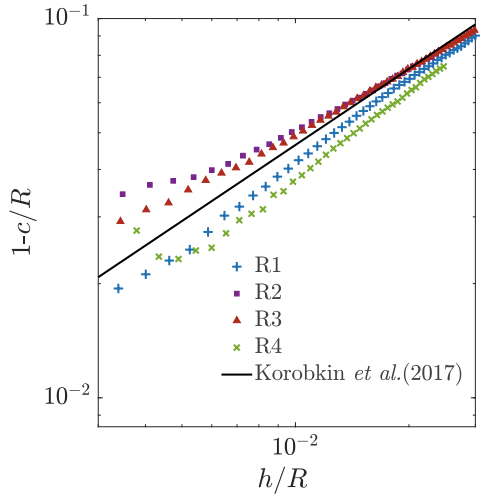

FIGURE 6.6. Log-log plot of $1 - c/R$ versus h_e/R, showing the convergence to the law $1 - c/R \sim (h_e/R)^{2/3}$ (solid line) predicted by Korobkin *et al.* (2017).

one decays whereas the other grows monotonically.

In the next sections we will show that the prediction of proportionality, equation (6.3), is based on the assumption that the plate is rigid. Once elastic effects are taken into account, the oscillatory behavior of the acceleration shown in figure 6.4b can be explained and quantitatively predicted.

6.3 Elastic effects on water exit

In order to explain the experimental results of the previous section, we assume that the hydroelastic interaction of the acrylic disc and the liquid is important during the early stage. This assumption is not obvious because the disc does not demonstrate visible elastic motions in the experiments. To prove that the disc elasticity is important in the water exit process, we generalize the linearised model of water exit of Korobkin (2013) by including the elasticity of the lifted body, and compare the obtained theoretical results with the experimental ones. The theoretical analysis is limited to axisymmetric problems, where the contact line remains attached to the edge of the plate, which corresponds to the conditions of the water exit in the present experiments during the early stage. Note that the connector is not axisymmetric in the experiments, see Figure 1b. Therefore, the experimental conditions are only approximately axisymmetric, and the disc deflection depends on the azimuthal coordinate, strictly speaking. However this effect is expected to be weak and negligible at leading order. In particular, the contact line in experiments, see Figure 3, is circular with good accuracy. Also, although we do not study the sensitivity of our experimental and theoretical results to a lack of axisymmetry, it will be shown in section 4.2, that even this approximately axisymmetric model accounting for the elasticity of the disc improves significantly the agreement between the theoretical and experimental results compared with the rigid body model of section 3.

6.3.1 Formulation of the axisymmetric exit problem and its solution

The problem of water exit is formulated in cylindrical coordinates (r, z), where r is the radial coordinate and z is the vertical one, which coincides with the symmetry axis of the plate. The plane $z = 0$ corresponds to the initial position of both the lower surface of the disc and the liquid surface, with the liquid occupying the lower half-space, $z < 0$. The disc touches the water surface with zero draft. Thus the initial position of the lower surface of the disc is $z = 0$, $r < R$. Then the disc is moved suddenly upwards by an external force applied at the disc centre. The position of the lower surface of the moving disc is described by the equation $z = w(r, t)$, where $w(r, t)$ accounts for both the rigid and elastic components of the disc displacement. During the early stage, when displacements are small compared to the disc radius R, the flow equations and the boundary conditions can be linearised. In particular, this means that the boundary conditions can be imposed on the initial position of the liquid boundary.

Under the assumptions of the early stage, the flow caused by lifting an elastic disc from the water surface is described by a velocity potential, $\varphi(r, z, t)$, which satisfies Laplace equation,

$$\frac{1}{r}\frac{\partial}{\partial r}\left(r\frac{\partial \varphi}{\partial r}\right) + \frac{\partial^2 \varphi}{\partial z^2} = 0 \qquad (z < 0), \tag{6.4}$$

in the initial flow region, the linearised dynamic condition on the free surface,

$$\varphi = 0 \qquad (z = 0, \quad r > R), \tag{6.5}$$

and the body boundary condition on the disc,

$$\frac{\partial \varphi}{\partial z} = \frac{\partial w}{\partial t} \qquad (z = 0, \quad r < R). \tag{6.6}$$

Furthermore, this potential decays at infinity, as $r^2 + z^2 \to \infty$.

The disc displacement, $w(r, t)$, is governed by the Bernoulli-Euler equation of thin elastic plates,

$$m\frac{\partial^2 w}{\partial t^2} + D\nabla^4 w = p_{ext}(r, t) + p_h(r, 0, t) \qquad (r < R, \quad t > 0), \tag{6.7}$$

where m is the mass of the disc per unit area, $m = \rho_p h_p$, D the rigidity coefficient, $D = Eh_p^3/[12(1-\nu^2)]$, for an elastic disc of constant thickness, see table 6.1 for the elastic constants of the disc material. The hydrodynamic pressure, $p_h(r, 0, t)$, acting on the disc/water interface, $z = 0$, is given by the linearised Bernoulli equation,

$$p(r, 0, t) = -\rho \varphi_t(r, 0, t), \tag{6.8}$$

whereas $p_{ext}(r, t)$ is the external load caused by the driving mechanism, see figure 6.1, and acting on the disc through the load cell and the connector. The external load is assumed uniformly distributed over a small circular area of radius r_c, $p_{ext}(r, t) = P(t)$, where $r < r_c$, with $F_{ext}(t) = \pi r_c^2 P(t)$ being the total force acting on the disc. Later, we will simplify the analysis by letting $r_c \to 0$. The displacement $w(r, t)$ is positive where the disc moves upwards. Note that different parts of the disc can move in different directions. For example, the centre of the disc may move upwards but the edge of the disc moves downwards at the same time. The bounday-value problem (6.4-6.8) is similar to that studied by Scolan (2004) for water entry of an elastic conical shell.

The connector is not axisymmetric in experiments. Therefore, the external load and the disc deflection should depend on the azimutal coordinate, strictly speaking. These azimutal modes are expected to introduce a high frequency jitter in the measured acceleration curves, although its amplitude must be small. Indeed, to trigger the non-axisymmetric modes in an efficient way, the force should be applied far from the disc centre, which is not the case here.

In the experiments, the weight of the connector, M_c, which is placed in between the load cell and the disc, is comparable with the weight, $M_p = \pi R^2 m$, of the disc. To account for this extra weight, Newton's second law for the connector,

$$M_c \frac{\partial^2 w}{\partial t^2}(0,t) = F_{exp}(t) - F_{ext}(t), \tag{6.9}$$

is used, where $F_{exp}(t)$ is the force measured by the load cell, and $-F_{ext}(t)$ is the force acting on the connector from the disc. We assume that the connector is rigidly connected to the centre of the disc, thus the displacement of the connector is approximately $w(0,t)$. Then the external load can be approximated by

$$p_{ext}(r,t) = \left(F_{exp}(t) - M_c \frac{\partial^2 w}{\partial t^2}(0,t) \right) \frac{\delta(r)}{2\pi r}, \tag{6.10}$$

where $\delta(r)$ is the Dirac delta function. In the present model, the force $F_{exp}(t)$ is assumed known from experimental measurements.

The disc edge, $r = R$, is free of stresses and shear forces. The radial bending moment and the Kelvin-Kirchhoff edge reaction are zero at the edge. For axisymmetric deflections of a circular plate, these two conditions read

$$\frac{\partial^2 w}{\partial r^2} + \frac{\nu}{r}\frac{\partial w}{\partial r} = 0, \qquad \frac{\partial}{\partial r}\left(\frac{1}{r}\frac{\partial}{\partial r}\left(r \frac{\partial w}{\partial r} \right) \right) = 0 \quad (r = R). \tag{6.11}$$

Initially, $t = 0$, both the disc and the water are at rest,

$$w(r,0) = 0, \quad w_t(r,0) = 0, \quad \varphi(r,z,0) = 0. \tag{6.12}$$

The problem formulated by equations (6.4)-(6.12) is coupled, the hydrodynamic loads and the disc displacement should be determined at the same time. The problem is solved by the normal mode method (Scolan, 2004; Khabakhpasheva & Korobkin, 1998; Korobkin, 2000; Khabakhpasheva, 2006; Khabakhpasheva *et al.*, 2013). Within this method the disc displacement is sought in the form

$$w(r,t) = h(t) + \sum_{n=1}^{\infty} a_n(t) W_n(\tilde{r}), \tag{6.13}$$

where $\tilde{r} = r/R$ is the non-dimensional radial coordinate, $\tilde{r} < 1$, $a_n(t)$ are the principal coordinates of the elastic deflections of the disc, which are to be determined, and $h(t)$ is the rigid-body displacement of the disc. The functions $W_n(\tilde{r})$ are the non-trivial bounded solutions to the homogeneous boundary value problem

$$\tilde{\nabla}^4 W_n = k_n^4 W_n \quad (\tilde{r} < 1), \tag{6.14}$$

$$W_n'' + \nu W_n' = 0, \quad (\tilde{\nabla}^2 W_n)' = 0 \quad (\tilde{r} = 1), \tag{6.15}$$

where

$$\tilde{\nabla}^2 W_n = \frac{1}{\tilde{r}}\frac{\partial}{\partial \tilde{r}}\left(\tilde{r}\frac{\partial W_n}{\partial \tilde{r}}\right), \tag{6.16}$$

a prime stands for the derivative in $\tilde{r}$, and k_n are the corresponding eigenvalues. The functions $W_n(\tilde{r})$, known as normal modes of the free-free circular elastic disc, describe the axisymmetric shapes of free vibrations of a circular disc with its edge being free of forces and bending stresses, and with frequencies proportional to k_n^2 (Leissa, 1969). The normal modes are orthogonal and read

$$W_n(\tilde{r}) = A_n\left(\mathrm{J}_0(k_n\tilde{r}) - \frac{\mathrm{J}_1(\mathrm{k_n})}{\mathrm{I}_1(\mathrm{k_n})}\mathrm{I}_0(\mathrm{k_n}\tilde{\mathrm{r}})\right), \tag{6.17}$$

where k_n , $n \geq 1$, are the positive solutions of the equation

$$\frac{\mathrm{J}_1(\mathrm{k_n})}{\mathrm{J}_0(\mathrm{k_n})} + \frac{\mathrm{I}_1(\mathrm{k_n})}{\mathrm{I}_0(\mathrm{k_n})} = \frac{2(1-\nu)}{k_n}, \tag{6.18}$$

and the coefficients A_n are determined by the normalization condition,

$$\int_0^1 W_n(\tilde{r})W_m(\tilde{r})\tilde{r}\mathrm{d}\tilde{r} = \delta_{nm}, \tag{6.19}$$

$\delta_{nm} = 0$ for $n \neq m$ and $\delta_{nn} = 1$. Equations (6.17)-(6.19) give

$$A_n = \left(\mathrm{J}_0^2(\mathrm{k_n}) - \frac{2\nu(1-\nu)}{\mathrm{k_n^2}}\mathrm{J}_1^2(\mathrm{k_n}) - \frac{2(1-\nu)}{\mathrm{k_n}}\mathrm{J}_0(\mathrm{k_n})\mathrm{J}_1(\mathrm{k_n})\right)^{-\frac{1}{2}}. \tag{6.20}$$

Note that

$$\int_0^1 W_n(\tilde{r})\tilde{r}\mathrm{d}\tilde{r} = 0, \tag{6.21}$$

which means that the elastic modes with $n \geq 1$ are orthogonal to the rigid mode, $W_0(\tilde{r}) = \sqrt{2}$, which corresponds to $k_0 = 0$.

The solution of the hydrodynamic problem (6.4)-(6.6) is given by

$$\varphi(R\tilde{r}, 0, t) = \int_{\tilde{r}}^1 \frac{\chi(\mu, t)\mathrm{d}\mu}{\sqrt{\mu^2 - \tilde{r}^2}}, \quad \chi(\mu, t) = \frac{2R}{\pi}\int_0^\mu \frac{w_t(R\sigma, t)\sigma\mathrm{d}\sigma}{\sqrt{\mu^2 - \sigma^2}}, \tag{6.22}$$

see Appendix A in Korobkin & Scolan (2006). It is convenient to introduce the functions $Q_n(x)$ and the coefficients W_{nk} by

$$Q_n(x) = \frac{1}{x}\int_0^x \frac{W_n(\sigma)\sigma\mathrm{d}\sigma}{\sqrt{x^2 - \sigma^2}}, \quad W_{nk} = \frac{2}{\pi}\int_0^1 x^2 Q_n(x)Q_k(x)\mathrm{d}x, \tag{6.23}$$

see Scolan (2004) and Pegg *et al.* (2018). In particular, $Q_0(x) = \sqrt{2}$. The functions $Q_n(x)$ and the coefficients W_{nk} are expressed through the Bessel, trigonometric and hyperbolic functions similar to those in Pegg *et al.* (2018), Appendixes B and C, where the corresponding integrals were evaluated for a simply supported circular elastic disc.

Substituting (6.13) in (6.22) and using (6.23) we find the velocity potential on the disc surface,

$$\chi(\mu,t)=\frac{2R}{\pi}\mu\left(h'(t)+\sum_{n=1}^{\infty}a_n'(t)Q_n(\mu)\right), \tag{6.24}$$

$$\varphi(R\tilde{r},0,t)=\frac{2R}{\pi}\left(h'(t)\sqrt{1-\tilde{r}^2}+\sum_{n=1}^{\infty}a_n'(t)\int_{\tilde{r}}^{1}\frac{\mu Q_n(\mu)\mathrm{d}\mu}{\sqrt{\mu^2-\tilde{r}^2}}\right). \tag{6.25}$$

The latter equation provides the asymptotic behaviour of the radial flow velocity near the edge of the disc,

$$\frac{\partial\varphi}{\partial r}(r,0,t)\sim-\frac{2RV(t)}{\sqrt{R^2-r^2}},\quad V(t)=h'(t)+\sum_{n=1}^{\infty}a_n'(t)Q_n(1). \tag{6.26}$$

Multiplying both sides of the plate equation (6.7) by $\tilde{r}$ and integrating in $\tilde{r}$ from 0 to 1 using (6.13), (6.10) and (6.21), we arrive at the following equation for the rigid displacement of the disc,

$$h''(t)=\frac{F_{exp}(t)}{M+m_a}-\sum_{n=1}^{\infty}a_n''(t)\left\{\frac{M_c}{M+m_a}W_n(0)+\frac{3\pi}{2\sqrt{2}}\frac{m_a}{M+m_a}W_{n0}\right\}, \tag{6.27}$$

where $M=M_c+M_p$ is the mass of the equipped disc, and m_a is the added mass of the disc (equation (6.2)). Equation (6.27) provides the acceleration at the disc centre, $a(t)$, which is measured in the experiments,

$$\begin{aligned}a(t)=\frac{\partial^2 w}{\partial t^2}(0,t)=h''(t)+\sum_{n=1}^{\infty}a_n''(t)W_n(0)=\frac{F_{exp}(t)}{M+m_a}+\\ \sum_{n=1}^{\infty}a_n''(t)\left\{\frac{M_p+m_a}{M+m_a}W_n(0)-\frac{3\pi}{2\sqrt{2}}\frac{m_a}{M+m_a}W_{n0}\right\}.\end{aligned} \tag{6.28}$$

Therefore, the elastic deflection of the disc may significantly affect the acceleration of its center. Formula (6.28) is reduced to (6.3) when the elastic accelerations are negligible, i.e. $a_k(t)\approx 0$.

The equations for elastic deflections of the disc follow from the plate equation (6.7). Multiplying both sides of the plate equation (6.7) by $\tilde{r}W_k(\tilde{r})$ and integrating in $\tilde{r}$ from 0 to 1 using (6.13), (6.10), (6.14) and (6.19), we arrive at the following equations for the principal coordinates $a_k(t)$, $k\geq 1$,

$$a_k''(t)+\omega_k^2 a_k=F_{exp}(t)f_k+\sum_{n=1}^{\infty}a_n''(t)S_{kn}, \tag{6.29}$$

where

$$\omega_n^2=\frac{Dk_n^4}{mR^4},\quad \gamma=\frac{3\pi}{2\sqrt{2}}\frac{m_a}{M+m_a},\quad f_k=\frac{M_p+m_a}{2M_p(M+m_a)}\left(W_k(0)-\gamma W_{k0}\right), \tag{6.30}$$

$$\begin{aligned}S_{kn}=S_{nk}=\frac{3\pi}{4\sqrt{2}}\frac{m_a}{M_p}\gamma W_{k0}W_{n0}-\frac{M_c}{2M_p}\frac{M_p+m_a}{M+m_a}W_k(0)W_n(0)\\ +\frac{\gamma M_c}{2M_p}\left(W_k(0)W_{n0}+W_n(0)W_{k0}\right)-\frac{3\pi}{4}\frac{m_a}{M_p}W_{nk}.\end{aligned} \tag{6.31}$$

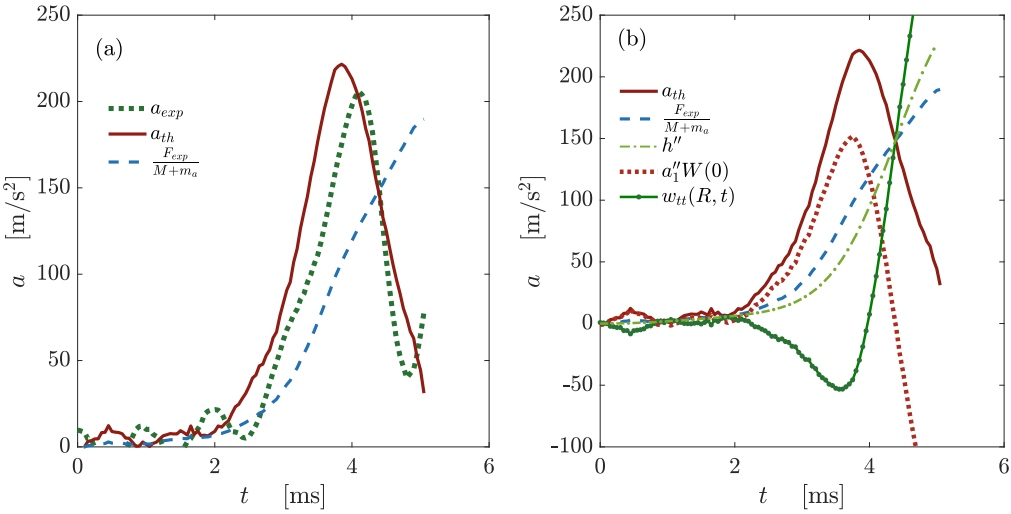

FIGURE 6.7. Comparison of experimental and theoretical results for session 3, repetition 1 (see figure 6.2). (a) Dashed line is for rigid wet-body acceleration $F_{exp}(t)/(M + m_a)$, solid line is for theoretical acceleration at the disc centre provided by equation (6.36), and the dotted line is for the measured acceleration. (b) rigid wet-body acceleration and theoretical acceleration measured at the center of the disc are the same as in (a), dash-dotted line is for the rigid-body acceleration $h''(t)$ given by (6.35), dotted line is for the elastic acceleration at the plate centre, $a_1''W_1(0)$, and the solid line with dots markers are for the acceleration of the disc edge, $w_{tt}(R, t)$.

The system (6.29) is integrated in time numerically subject to the initial conditions

$$a_k(0) = 0, \quad a_k'(0) = 0 \quad (n \geq 1) \tag{6.32}$$

and for the forcing function $F_{exp}(t)$ measured in the experiments. Then the acceleration at the center of the disc is calculated using equation (6.28) and compared with the results gathered by the accelerometer.

6.3.2 Comparison between theoretical and experimental results

The computations are performed for the one-mode approximation with $a_k(t) \equiv 0$ for $n \geq 2$. This is because the conditions of the experiments are axisymmetric only approximately. Therefore, we do not expect that including more axisymmetric terms in the series (6.13) would improve the theoretical predictions of the disc acceleration compared to the experimental ones.

For the conditions of the experiments with the plate thickness $h_p = 1$ cm (see table 6.1) we calculate $k_1 = 3.011$. The frequency and the period of the first dry mode are $\omega_1 = 3853$ s^{-1} and $T_1 = 1.63$ ms. (Compare with the corresponding values for the second dry elastic mode, $k_2 = 6.2$, $\omega_2 = 16363$ s^{-1}, $T_2 = 0.38$ ms), $\gamma = 2.423$, and $W_{10} = 0.143$, $W_1(0) = 2.848$, $W_{11} = 0.218$, $f_1 = 2.645$ kg^{-1}, $S_{11} = -2.921$. The resulting equation for the principal coordinate of the first elastic mode reads

$$a_1''(t) + \Omega_1^2 a_1 = \alpha_1 F_{exp}(t), \tag{6.33}$$

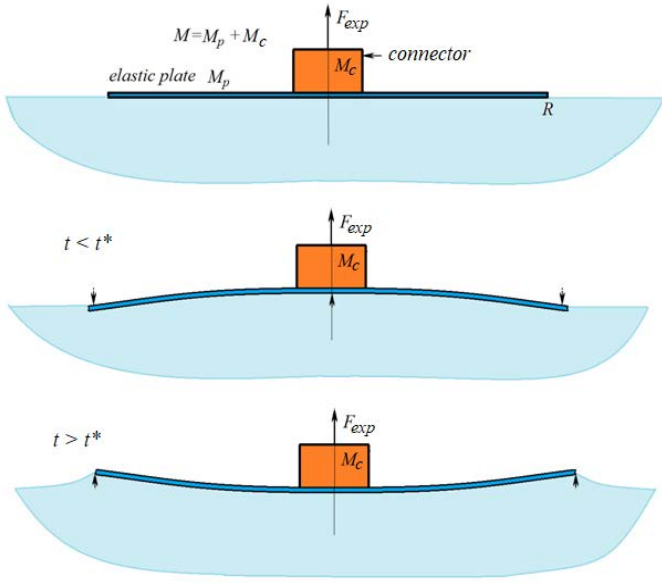

FIGURE 6.8. Sketch of the expected motion during the initial stages of the elastic disc lifting from the water surface.

where the frequency of the first wet mode, Ω_1, and the forcing factor α_1 are given by

$$\Omega_1 = \frac{\omega_1}{\sqrt{1 - S_{11}}}, \qquad \alpha_1 = \frac{f_1}{1 - S_{11}}. \tag{6.34}$$

In the conditions of these experiments, $\Omega_1 = 1946$ sec^{-1} and $\alpha_1 = 0.675$ kg^{-1}. The corresponding period of the first wet elastic mode is equal to $2\pi/\Omega_1 = 3.223$ ms, which is twice greater than the period of the dry mode, and is comparable with the peak time of the measured acceleration, see figures 6.7 and 6.10. Equation (6.33) is integrated numerically for the function $F_{exp}(t)$ measured by the load cell and the initial conditions (6.32). Then the acceleration of the rigid body motion of the disc is calculated by (6.27), which reads within the one-mode approximation,

$$h''(t) = \frac{F_{exp}(t)}{M + m_a} - \alpha_2\, a_1''(t), \quad \alpha_2 = \frac{M_c}{M + m_a} W_1(0) + \gamma W_{10}. \tag{6.35}$$

The theoretical acceleration of the disc centre, $a(t)$, is calculated by equation (6.28),

$$a(t) = \frac{F_{exp}(t)}{M + m_a} + \alpha_3\, a_1''(t), \quad \alpha_3 = \frac{M_p + m_a}{M + m_a} W_1(0) - \gamma W_{10}. \tag{6.36}$$

For the conditions of our experiments, $\alpha_2 = 0.59$ and $\alpha_3 = 2.61$. Therefore, the effect of the elastic deflection of the disc on the rigid motion of the disc is about four times smaller than on the acceleration of the disc centre.

Figure 6.7a compares the measured acceleration of the disc centre (dotted line) with the theoretical predictions (equation 6.36) (solid line) for the first run of session 3. The first

term in (6.36) is shown by the solid thin line. Therefore we can claim that accounting for the disc elasticity explains the relation between the measured force and acceleration. More details about the disc motion are shown in figure 6.7b. It can be observed that the rigid-solid component of the acceleration $h''(t)$ (dash-dotted line) depends weakly on the elasticity of the disc and is close to the acceleration predicted by the rigid disc model (equation (6.2), dashed line. The total acceleration of the disc centre (solid line), $a(t)$, is the sum of two components within the one-mode approximation, $a(t) = h''(t) + a_1''(t)W_1(0)$, see equation (6.28). The elastic acceleration, $a_1''(t)W_1(0)$, is shown by the dotted line. It is larger than the rigid acceleration, $h''(t)$, for $0 < t < 4$ ms. The acceleration of the disc edge, $w_{tt}(R,t) = h''(t) + a_1''(t)W_1(1)$, is shown by the solid line with dots markers. It is seen that this acceleration is negative for $0 < t < 3.8$ ms. Therefore, initially the edge of the disc goes down but the disc centre goes up. This situation is sketched in figure 6.8. The edge of the plate moves down when $0 < t < t^*$, where t^* is determined by the equation $w_t(R,t^*) = 0$. The calculations provide $t^* = 4.5$ ms for the case of figure 6.7. Initially the edge of the disc penetrates the water even though the main part of the disc exits the water. The radial velocity of the flow near the disc edge is given by equation (6.26). Within the one-mode approximation, the vertical velocity of the disc edge,

$$w_t(R,t) = h'(t) + a_1'(t)W_1(1), \tag{6.37}$$

the coefficient $V(t)$ in (6.26),

$$V(t) = h'(t) + a_1'(t)Q_1(1), \tag{6.38}$$

and the coefficient,

$$U(t) = -h''(t) - a_1''(t)Q_1(1), \tag{6.39}$$

in the asymptotic formula for the pressure,

$$P(r,0,t) \sim \frac{2\rho}{\pi}U(t)\sqrt{R^2 - r^2} \qquad (r \to R - 0), \tag{6.40}$$

near the contact line before it starts to move are depicted in figure 6.9. Physically speaking the contact line cannot move if the pressure under the disc edge is greater than the atmospheric pressure, when $U(t)$ given by equation (6.39) is positive, see equation (6.40). The calculations provide that $U(t)$ is very close to zero for $0 < t < 4$ ms and quickly decreases after this time. The contact line does not move also if the radial velocity of the flow at the disc edge is positive, $V(t)$ given by equation (6.38) is negative, see equation (6.26). The calculations show that $V(t)$ is positive but very small for $0 < t < 3$ ms. The disc edge moves down for $0 < t < 4.6$ ms, see line 1 in figure 6.9b. Therefore figure 6.9 shows that the generalised exit theory predicts that the contact line is unlikely to move before $t = 3.5 - 4$ ms which is in good agreement with the experiments (see figure 6.5a).

The theoretical accelerations $a(t)$ calculated for different forcing functions $F_{exp}(t)$ in different experimental runs are compared with the measured accelerations in figure 6.10. These results confirm that taking into account the elastic deflection of the disc explains the non-monotonic relation between the measured forces and measured accelerations. The discrepancies between the peak accelerations derived theoretically and measured experimentally shown in figure 6.10 are 13.47% for panel (a), 17.72% for (b), and 6.59% for (c). The repetition shown in figure 6.10d corresponds to a drop that felt from a lower height, compared to the other runs. Thus, the force applied to pull up the disc was smaller

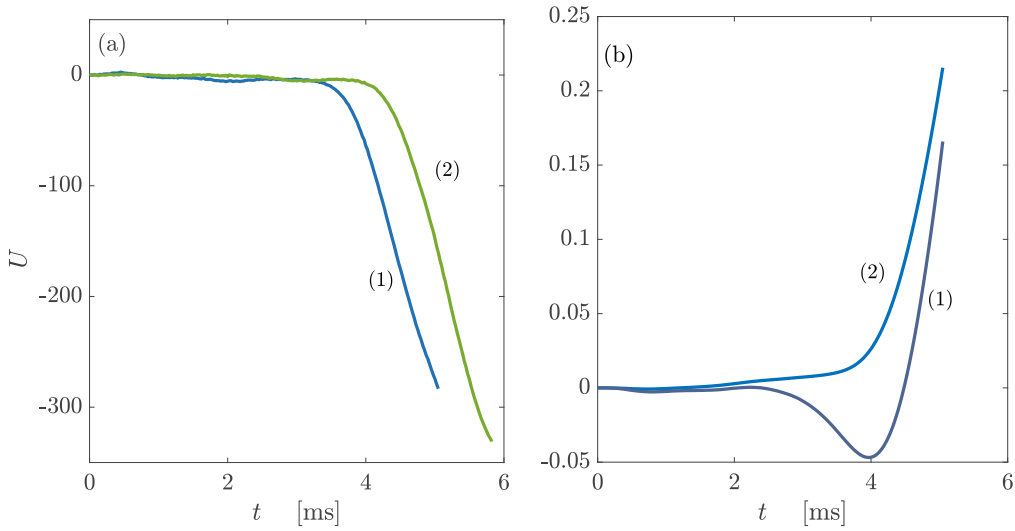

FIGURE 6.9. (a) Pressure coefficients $U(t)$ for two repetitions of session 3 (1 and 2). (b) $w_t(R,t)$ (line 1) and $V(t)$ (line 2) for session 3, repetition 1.

and so was the acceleration. Nonetheless the agreement between the theory and experiments is still good even in these different conditions (the discrepancy in this case is 11.35%). Even though the specific details of the measured forces and accelerations are rather sensitive to the precise initial conditions of each run, the theory predicts well the maximum accelerations and their duration.

To prove that elastic effects are negligible in the absence of water, we show in figure 6.11 the acceleration $a_{exp}(t)$ measured by the accelerometer, the acceleration computed from the load-cell measurements under the rigid-body assumption, $F_{exp}(t)/M$, and the acceleration predicted by the present elastic model, $a_{th}(t)$, with $m_a = 0$. It is seen that all these three accelerations are close to each other, with the maximum difference between them being 5.5%.

To conclude this subsection, a few comments can be made about the distribution of stresses in the disc. The radial σ_r and tangential σ_t stresses on the disc surface are given by

$$\sigma_r(R\tilde{r},t) = \frac{Eh_p}{2R^2(1-\nu^2)}\Big(W_1''(\tilde{r}) + \frac{\nu}{\tilde{r}}W_1'(\tilde{r})\Big)a_1(t), \tag{6.41}$$

$$\sigma_t(R\tilde{r},t) = \frac{Eh_p}{2R^2(1-\nu^2)}\Big(\nu W_1''(\tilde{r}) + \frac{1}{\tilde{r}}W_1'(\tilde{r})\Big)a_1(t), \qquad (\tilde{r}<1), \tag{6.42}$$

in the one-mode approximation. For the conditions of figure 6.7, the theoretical amplitude of the elastic mode $a_1(t)$ increases monotonically from zero to 4×10^{-4} mm at the end of the measurements. The functions $\tilde{\sigma}_r(\tilde{r}) = W_1''(\tilde{r}) + \nu W_1'(\tilde{r})/\tilde{r}$ and $\tilde{\sigma}_t(\tilde{r}) = \nu W_1''(\tilde{r}) + W_1'(\tilde{r})/\tilde{r}$ are shown in figure 6.12. Their maximum values are achieved at $\tilde{r} = 0$ and are equal to each other.

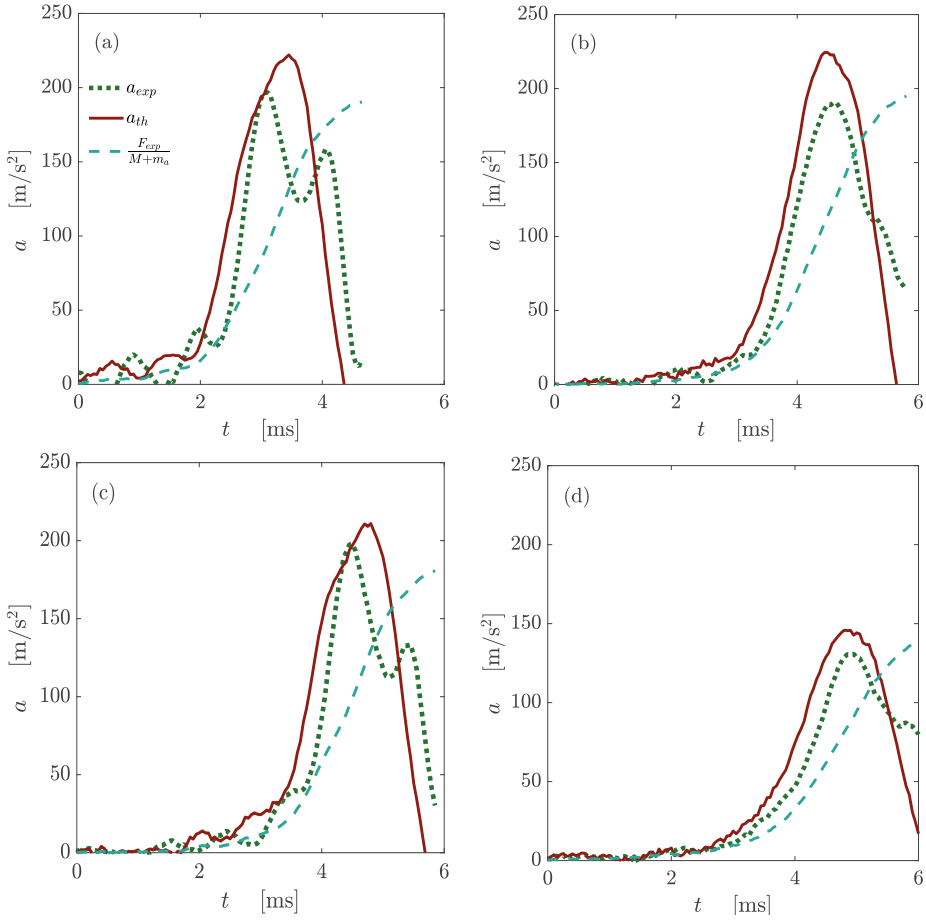

FIGURE 6.10. Comparison of the theoretical accelerations at the disc centre with the experimental ones for four runs (session 3, repetitions 2, 3, 4, and 5). Dashed lines represent the rigid wet-body acceleration, $F_{exp}(t)/(M + m_a)$, solid lines the theoretical accelerations at the disc centre provided by equation (6.28) and the dotted lines are for the measured accelerations.

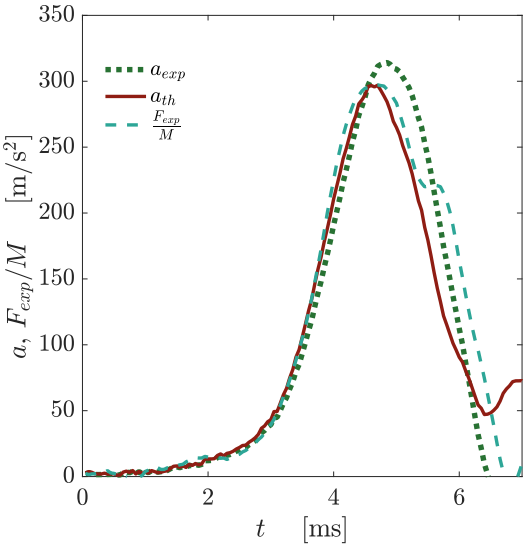

FIGURE 6.11. Comparison of the measured acceleration, a_{exp}, the acceleration computed using the load-cell measurements under the rigid-body assumption, F_{exp}/M, and the theoretical acceleration, a_{th}.

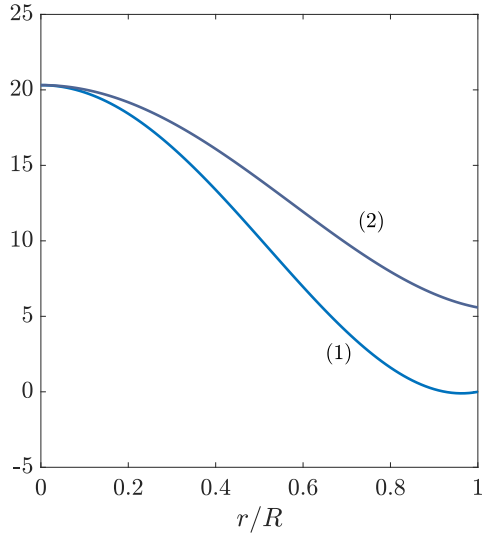

FIGURE 6.12. Distributions of radial and tangential normalised stresses along the disc radius, curve (1) corresponds to $\tilde{\sigma}_r(\tilde{r})$ and (2) to $\tilde{\sigma}_t(\tilde{r})$.

h_p (cm)	M_p (kg)	M (kg)	$\omega_{wet,1}$ (s^{-1})	$T_{wet,1}$ (ms)
0.5	0.216	0.414	775	8.10
1	0.432	0.630	1945	3.23
2	0.864	1.07	5034	1.25

TABLE 6.3. Properties of the three different discs used in experiments.

6.3.3 Effect of plate thickness

To further support the conclusion that elastic effects are essential during the initial stages of the plate exit, we provide here additional experiments with two discs of thicknesses $h_p = 0.5$ cm and $h_p = 2$ cm, see table 6.3. As expected, the elastic vibrations of the thicker disc have smaller amplitude and higher frequency than those of the thinner one, as depicted in figure 6.13. In general, the period of these oscillations is reasonably well captured by the theory. It should be stressed that the results presented here have been obtained using the measured properties of the plates and that, once these parameters are fixed, the theory has no adjustable parameters and its only input is the excitation force measured experimentally.

For the thinner plate, the first peak of the acceleration is very well described by the theory, as illustrated in figure 6.14, albeit the second one exhibits an amplitude substantially smaller than the calculated one. We hypothesize that this disagreement is caused by several effects. First, it should be reminded that, in the theory, we assume that the force is applied at the center, whereas in reality it is applied on a non-axisymmetric region. Second, non-linearity leads to the appearance of higher-order modes, including non-axisymmetric ones, which are excited more easily in a thinner plate, since their –longer– natural period is closer to the duration of the experiment. A third explanation may be sought in the fact that our theory does not account for any source of dissipation. Due to the smaller elastic energy stored in a thin plate, the effects of dissipation are expected to be more important in relative terms. Finally, because of its smaller mass, a thin plate leaves the water surface at a slightly larger acceleration than a heavier one, thus the assumption that the virtual mass is that evaluated at $t = 0$ becomes questionable. In figure 6.14, the maximum difference between the theoretical and experimental accelerations is 19.5%, but the difference between the measured and the rigid wet-body accelerations is 400%, which shows that the rigid-disc model of water exit is not applicable to the case of this thin disc.

Regarding the results for the thick plate, $h_p = 2$ cm (see figure 6.15), the theory predicts accelerations which oscillate around the experimental ones, albeit with a larger amplitude, which we attribute again to the lack of dissipation in the model. The maximum difference between the theoretical and the experimental acceleration is 33% in figure 6.15c. For the other cases these differences are smaller than 13%. Despite this discrepancy, the period of these oscillations is well predicted by the elastic exit theory. Note that these oscillations are not present in the rigid wet-body accelerations shown by dashed lines in figure 6.15. Thus, we find fair to state that the elastic theory predicts better the experimental behavior in this case. Indeed, for a thick plate we expect the arguments used in the previous paragraph for a thin plate to reverse, which explains the better agreement between theory and experiments.

In view of these results, we find reasonable to claim that the generalised linear theory of water exit presented here can be successfully used to describe the motions of an elastic body that leaves the water surface at a large acceleration, such that its elastic vibrational modes are excited.

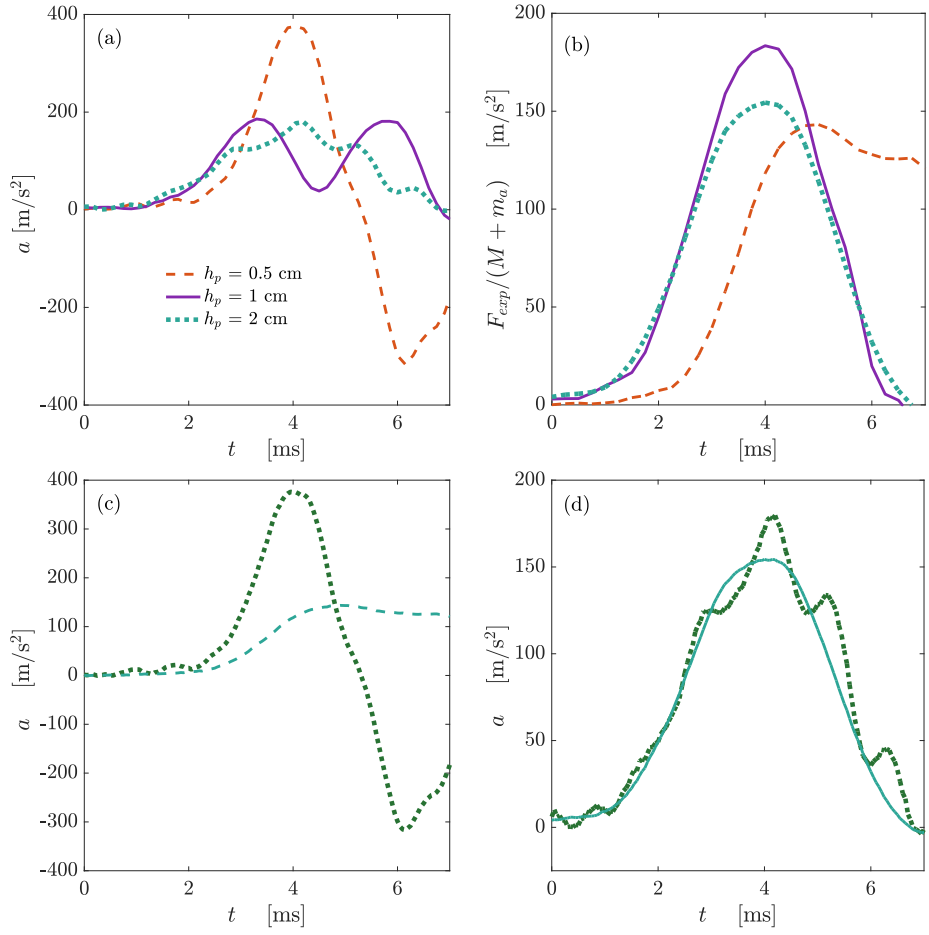

FIGURE 6.13. Comparison of the experimental accelerations at the disc centre (a) and the measured rigid wet-body accelerations, $F_{exp}(t)/(M + m_a)$, (b), for three different plate thicknesses, 0.5, 1, and 2 cm. Comparison between the experimental accelerations (dotted lines) and the rigid wet-body accelerations, $F_{exp}(t)/(M + m_a)$, (dashed lines) for the plate thicknesses $h_p = 0.5$ cm (c) and $h_p = 2$ cm (d).

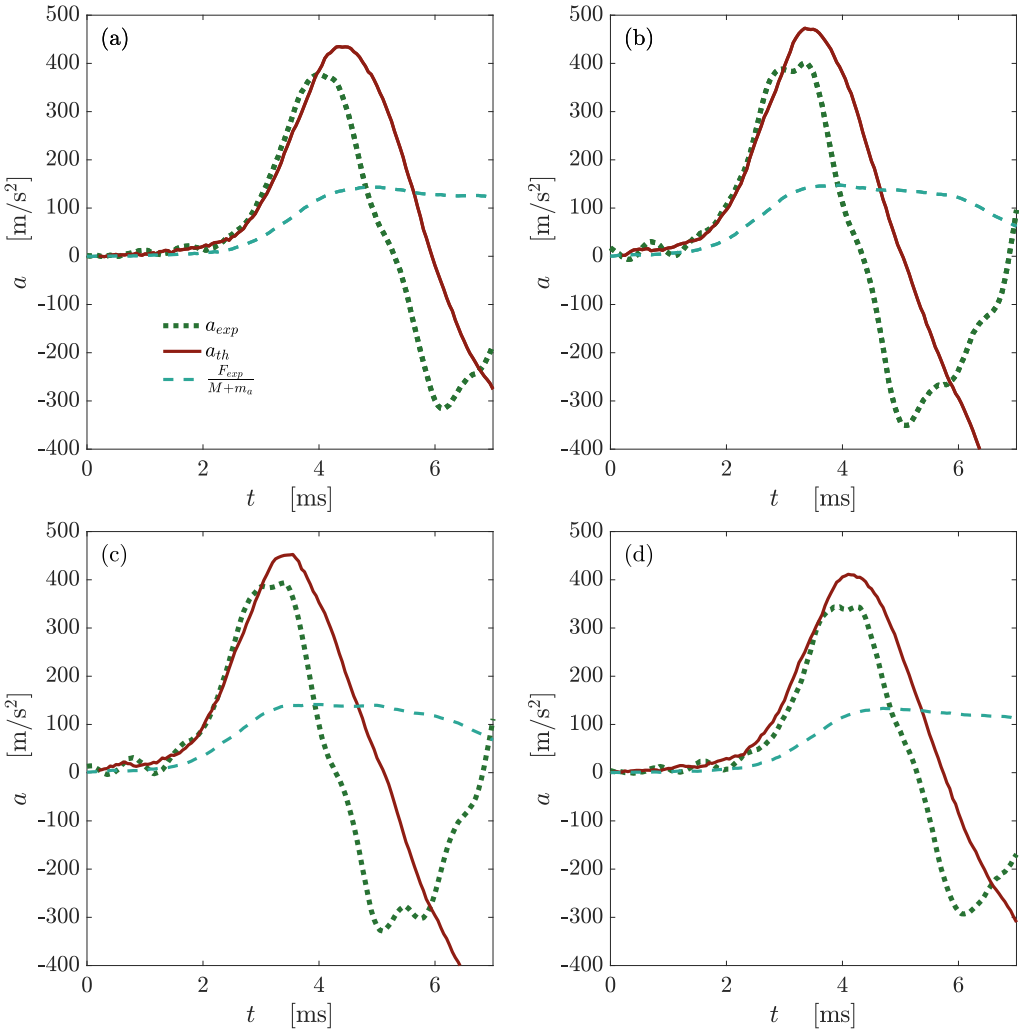

FIGURE 6.14. Comparison of theoretical accelerations at the disc centre with the experimental ones (session 5) in four runs for disc thickness, $h_p = 0.5$ cm. Dashed lines are for the rigid wet-body acceleration, $F_{exp}(t)/(M + m_a)$, solid lines are for the theoretical accelerations at the disc centre provided by equation (6.28) and dotted lines are for the measured acceleration.

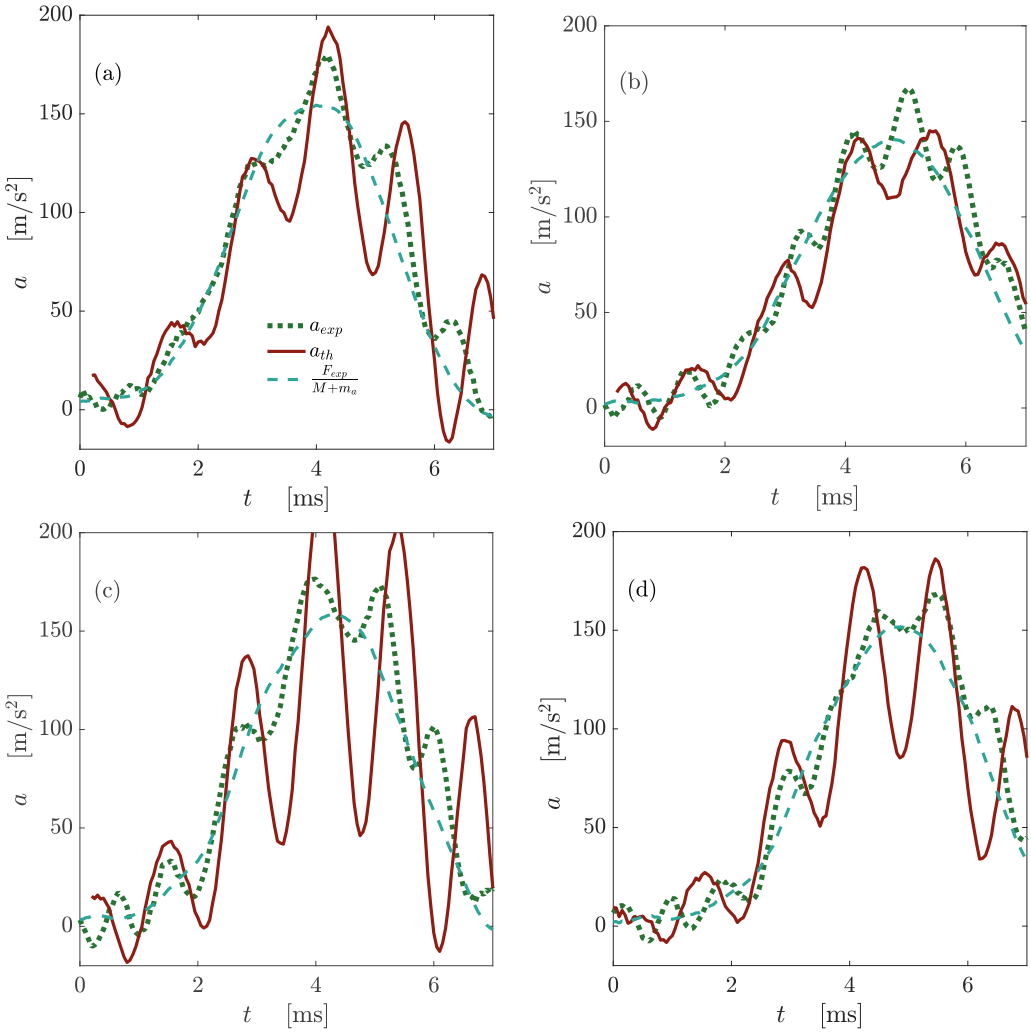

FIGURE 6.15. Comparison of theoretical accelerations at the disc centre with the experimental ones (session 4) in other four runs for disc thickness, $h_p = 2$ cm. See figure 6.14 for an explanation of the different curves.

Acknowledgements

This work was supported by the Spanish Ministry of Economy and Competitiveness through grants DPI2014-59292-C3-1-P, DPI2015-71901-REDT, and DPI2017-88201-C3-3-R, partly funded by Europan funds, and the NICOP research grant "Vertical penetration of an object through broken ice and floating ice plate" N62909-17-1-2128, through Dr. Salahuddin Ahmed. We also thank Dr. L. Champougny for her valuable comments on the manuscript, and David, Manuel and Israel for their work in the experimental installation.

CHAPTER 7

Conclusions

We designed, built and tested a facility to investigate the sudden lifting of a plate from a water surface. The results of the experimental campaign carried out in this facility for a circular plate, a disc, have been presented and analysed using the added mass theory. Several non-intuitive phenomena have been observed in the experiments. First the acceleration of the plate close to the place where the external force is applied does not monotonically increase in time even if the external force does. Second, the wetted part of the plate does not start instantaneously to decrease with the plate lifting. Instead, there is an initial interval of time during which the wetted part of the plate does not shrink. It was found that both these phenomena are governed by the elastic properties of the plate and the interaction between the liquid flow and the plate deflection.

It was inferred from these observations that the modelling of the suction force experienced by a rigid plate that leaves a water surface at a large acceleration is complex, due to the interplay between the body motion and the free surface dynamics. Nonetheless, at the very early stages of the motion this modelling was greatly simplified by linearizing the equations and boundary conditions through exploiting the fact that the displacements of the body and the water surface are very small. In particular, this allowed us to impose the boundary conditions at the undisturbed (flat and horizontal) free surface and initial body position. The linearised exit theory of rigid bodies (Korobkin, 2013) predicts that the body acceleration is proportional to the driving force, where the proportionality coefficient depends on the added mass of the body.

Although at very short times this approach yields reasonable results, as was shown for instance by the numerical simulations of Korobkin *et al.* (2017*a*) as well as by our experimental observations (see figure 6.4b), eventually the acceleration predicted by the theory significantly departs from the acceleration at the center of the plate obtained experimentally. Most notably, the observed accelerations even decrease in response to a monotonically increasing force.

This disagreement has motivated the development of a generalised linear theory of water exit that takes into account the elastic response of the plate to large accelerations. This new theory is based on the same ideas of Korobkin (2013) but includes, for the first time, the deformation dynamics of the plate through the linear elastic theory of thin plates.

Taking advantage of the linear nature of both the hydrodynamic and elastic problems, the disc displacement was expressed as a series of normal elastic modes of a free-free circular disc supported at its center. The theoretical results obtained with only one mode agree fairly

well with experiments, while keeping the complexity of the solution at a reasonable level. We stress here again that this theory has no free parameters to adjust, and all the required inputs are determined experimentally.

Besides yielding accelerations close to the experimental ones, the hydroelastic theory of water exit predicts that the contact line between the liquid, the air and the plate will remain attached initially to the edge during several milliseconds, which is also in excellent agreement with our observations using high-speed movies. It is also interesting to point out here that, once the contact line detaches from the plate edge, it recoils as the plate instantaneous height raised to the power of 2/3, as predicted by the self-similar solution obtained by Korobkin *et al.* (2017*b*) for the flow close to the corner of a plate leaving a water surface at a large acceleration. It is worth highlighting that these features of the flow near the edge are well described with the theory, despite the fact that the pressure field underneath the plate is calculated with the assumption of fixed contact radius, $c = R$. The reason for this is that, as pointed out in Korobkin *et al.* (2017*b*), the flow motion in a region close to the contact line is determined by the pressure distribution far away from the edge, where the suction created by the plate lifting is maximum. Therefore, the details of the flow near the corner do not affect substantially the pressure distribution.

We would like to highlight the surprising result that seemingly stiff plates like the ones used in our experiments, exhibit elastic effects strong enough to completely alter their surface exit dynamics. We show that the additional local inertia caused by the liquid motion is responsible for this elastic behavior. This effect was not observed in those experiments where the plate does not touch the water, see figure 6.11. In these cases, the acceleration and the applied force nearly follow each other within the experimental error margin.

Despite the generally good agreement with the experiments, our theoretical model still exhibits some discrepancies, specially for small plate thicknesses. We attribute those to: (a) the non-axisymmetric way in which the force is applied to the disc in the experiments, (b) the appearance of higher-order and non-asisymmetric modes, not considered in our calculations, (c) the absence of a dissipation mechanism that surely exists in the experiments, and (d) the assumption that the disc surface remains completely wet at all times.

Even taking into account the assumptions just mentioned, we believe that it is fair to conclude that the hydroelastic theory presented here emerges as a simple yet useful tool to compute the fluid-structure interaction in water exit phenomena occurring at large accelerations.

References

References

Baarholm, R. 2001 A boundary-element method for solving water impact on a platform deck. In *Proceedings of the 20th Offshore and Arctic Engineering Conference (OMAE 2002), New York*. ASME.

Baarholm, R. & Faltinsen, O. M. 2004 Wave impact underneath horizontal decks. *Journal of marine science and technology* **9** (1), 1–13.

Colicchio, G., Greco, M., Miozzi, M. & Lugni, C. 2009 Experimental and numerical investigation of the water-entry and water-exit of a circular cylinder. . . . *24th Int. Work.* . . . pp. 2–5.

Faltinsen, O. M., Landrini, M. & Greco, M. 2004 Slamming in marine applications. *Journal of Engineering Mathematics* **48** (3-4), 187–217.

Greenhow, M. 1988 Water-entry and-exit of a horizontal circular cylinder. *Applied Ocean Research* **10** (4), 191–198.

Greenhow, M. & Lin, W.-M. 1983 Nonlinear Free Surface Effects: Experiments and Theory p. 103.

Iafrati, A. & Korobkin, A. A. 2004 Initial stage of flat plate impact onto liquid free surface. *Phys. Fluids* **16** (7), 2214–2227.

Iafrati, A. & Korobkin, A. A. 2008 Hydrodynamic loads during early stage of flat plate impact onto water surface. *Physics of Fluids* **20** (8), 082104.

Ioannou, Dimitrios, Huda, Walter & Laine, Andrew F 1999 Circle recognition through a 2d hough transform and radius histogramming. *Image and vision computing* **17** (1), 15–26.

Khabakhpasheva, T. I. 2006 Impact of a surfacewave on an elastic hull. *Fluid Dynamics* **41**, 424–433.

Khabakhpasheva, T. I. & Korobkin, A. A. 1998 Plane problem of asymmetrical wave impact on an elastic plate. *Journal of Applied Mechanics and Technical Physics* **39**, 782–791.

Khabakhpasheva, T. I., Korobkin, A. A., Maki, K. J. & Seng, S. 2016 Water entry and exit with large displacements by simplified models. In *Proceedings of the 31 St International Workshop on Water Waves and Floating Bodies, Michigan, USA*.

Khabakhpasheva, T. I., Korobkin, A. A. & Malenica, S. 2013 Fluid impact onto a corrugated panel with trapped gas cavity. *Applied Ocean Research* **39**, 97–112.

Korobkin, A. A. 2000 Unsteady hydroelasticity of floating plates. *Journal of Fluids and Structures* **14**, 971–991.

Korobkin, A. A. 2004 Analytical models of water impact. *European Journal of Applied Mathematics* **15** (6), 821–838.

Korobkin, A. A. 2013 A linearized model of water exit. *Journal of Fluid Mechanics* **737**, 368–386.

Korobkin, A. A., Khabakhpasheva, T. I. & Maki, K. J. 2014*a* Water-exit problem with prescribed motion of a symmetric body. In *Proceedings 29th International Workshop on Water Waves and Floating Bodies, Japan*.

Korobkin, A. A., Khabakhpasheva, T. I. & Maki, K. J. 2017*a* Hydrodynamic forces in water exit problems. *Journal of Fluids and Structures* **69**, 16–33.

Korobkin, A. A., Khabakhpasheva, T. I. & Rodríguez-Rodríguez, J. 2017*b* Initial stage of plate lifting from a water surface. *Journal of Engineering Mathematics* **102** (1), 117–130.

Korobkin, A. A., Maki, K., Rodríguez-Rodríguez, J. & Khabakhpasheva, T. I. 2014*b* Oscillations of an elastically supported body in partial contact with water. *17th U.S. National Congress on Theoretical and Applied Mechanics* pp. C–08–506.

Korobkin, A. A. & Pukhnachov, V. V. 1988 Initial stage of water impact. *Annual Review of Fluid Mechanics* **20**, 159–185.

Korobkin, A. A. & Scolan, Y.-M. 2006 Three-dimensional theory of water impact. Part 2. Linearized Wagner problem. *Journal of Fluid Mechanics* **549**, 343–373.

Leissa, A. W. 1969 Tabulated numerical results of theories of plate vibration. *NASA Technical Report, NASA-SP-160* .

Moyo, S. & Greenhow, M. 2000 Free motion of a cylinder moving below and through a free surface. *Appl. Ocean Res.* **22** (1), 31–44.

Pegg, M., Purvis, R. & Korobkin, A. A. 2018 Droplet impact onto an elastic plate: a new mechanism for splashing. *Journal of Fluid Mechanics* **839**, 561–593.

Piro, D. J. & Maki, K. J. 2011 Hydroelastic wedge entry and exit. In *11th International Conference on Fast Sea Transport. Honolulu, Hawaii, USA*.

Piro, D. J. & Maki, K. J. 2012 Water exit of a wedge-shaped body. In *Proceedings 27th IWWWFB, Copenhagen*.

Piro, D. J. & Maki, K. J. 2013 Hydroelastic analysis of bodies that enter and exit water. *Journal of Fluids and Structures* **37**, 134–150.

Rajavaheinthan, R. & Greenhow, M. 2015 Constant acceleration exit of two-dimensional free-surface-piercing bodies. *Applied Ocean Research* **50**, 30–46.

Reis, P. M., Jung, S., Aristoff, J. M. & Stocker, R. 2010 How cats lap: water uptake by felis catus. *Science* **330** (6008), 1231–1234.

Scolan, Y.-M. 2004 Hydroelastic behaviour of conical shell impacting on a quiescent-free surface of an incompressible liquid. *Journal of Sound and Vibration* **277**, 163–203.

Scolan, Y.-M. & Korobkin, A. A. 2001 Three-dimensional theory of water impact. Part 1. Inverse Wagner problem. *Journal of Fluid Mechanics* **440**, 293–326.

Scolan, Y.-M. & Korobkin, A. A. 2003 Energy distribution from vertical impact of a three-dimensional solid body onto the flat free surface of an ideal fluid. *Journal of Fluids and Structures* **17**, 275–286.

Scolan, Y.-M., Remy, F. & Thibault, B 2006*a* Impact of three-dimensional standing waves on a flat horizontal plate. In *21st International Workshop on Water Waves and Floating Bodies, Loughborough, UK*.

Scolan, Y.-M., Remy, F. & Thibault, B. 2006*b* Impact of three-dimensional standing waves on a flat horizontal plate. In *21st International Workshop on Water Waves and Floating Bodies*.

Tassin, A., Breton, T., Forest, B., Ohana, J., Chalony, S., Roux, D. Le & Tancray, A. 2017*a* Visualization of the contact line during the water exit of flat plates. *Experiments in Fluids* **58** (8), 104.

Tassin, A., Breton, T. & Jacques, N. 2017*b* Evolution of the contact line during the water exit of flat plates. In *Proceedings of 32nd International Workshop on Water Waves and Floating Bodies*.

Tassin, A., Breton, T. & Jacques, N. 2018*a* Experimental and theoretical study on the water entry and water exit phenomena. In *Proceedings of 16 èmes Journées de l'Hydrodynamique, Marseille, France*.

Tassin, A., Jacques, N. & Breton, T. 2018*b* Experiments on the water entry and/or exit of a cone. In *International Workshop on Water Waves and Floating Bodies (IWWWFB)*.

Tassin, A., Piro, D. J., Korobkin, A. A., Maki, K. J. & Cooker, M. J. 2013 Two-dimensional water entry and exit of a body whose shape varies in time. *Journal of Fluids and Structures* **40**, 317–336.

Taubin, G. 1991 Estimation of Planar Curves, Surfaces, and Nonplanar Space Curves Defined by Implicit Equations with Applications to Edge and Range Image Segmentation **13** (11).

Vega-Martínez, Patricia, Rodríguez-Rodríguez, Javier, Khabakhpasheva, TI & Korobkin, AA 2019*a* Hydroelastic effects during the fast lifting of a disc from a water surface. *Journal of Fluid Mechanics* **869**, 726–751.

Vega-Martínez, P, Rodríguez-Rodríguez, J, Khabakhpasheva, TI & Korobkin, AA 2019*b* Hydroelastic effects during the fast lifting of a disc from a water surface–corrigendum. *Journal of Fluid Mechanics* **878**, 932–933.

Von Karman, T. 1929 The impact on seaplane floats during landing. *NACA Technical Note 321* pp. 309–311.

Yuen, HK, Princen, John, Illingworth, John & Kittler, Josef 1990 Comparative study of hough transform methods for circle finding. *Image and vision computing* **8** (1), 71–77.

Zhu, X., Faltinsen, O. M. & Hu, C. 2007 Water Entry and Exit of a Horizontal Circular Cylinder. *J. Offshore Mech. Arct. Eng.* **129** (4), 253.

Agradecimientos

Defiende tu derecho a pensar, porque incluso pensar de manera errónea es mejor que no pensar.

– Hipatia de Alejandría (355/370 - 415/416)

Probablemente, esta sea la página más leída de la tesis.

Aquí se aplica la propiedad conmutativa: el orden de los factores no altera el producto. Javi, muchas gracias por todo lo que me has enseñado durante estos cuatro años, por ayudarme siempre que lo he necesitado, por tu apoyo, tu entusiasmo ante cualquier reto, tu paciencia, por la confianza que has puesto en mí y la que me has hecho ganar poco a poco, en definitiva por estar ahí no solo como advisor (se que te gusta más en inglés ;)). Porque hemos formado un gran equipo y esta tesis lo avala. Para mí, junto con Pablo Peñas, sois unos genios. Pablo, aunque ya no estés por la uni, muchas gracias por explicarme cada cosa las veces que hiciera falta, por los momentos soldando tantos sensores de presión y por tu risa inconfundible, trabajar contigo ha sido un lujo. A Manolo, Isra y David, sin vosotros estas instalaciones experimentales no serían lo que son, y no solo por vuestro brillante trabajo sino también por todos esos momentos de risas y conversaciones. Ferni y María (little chicken), que os voy a decir yo a vosotros que no sepáis ya, si somos el trio–lalala, solo nos falta hacernos camisetas (¡Ferni para tu defensa las tenemos!). Simplemente gracias por estar siempre ahí, por todos esos momentitos y momentazos dentro y fuera de la uni. A mis compis de despacho, Alejandro, Dani (Gómez) y Vanesa, uno durante los primeros años, otra durante el último y otro desde el principio al final. Por todos los buenos ratos, los cambios de despacho, los dramas y las conversaciones con y sin sentido. En especial a ti, Alejandro, porque siempre me has ayudado y aconsejado aunque no siempre te haya hecho caso. A Jesús, Marta, Rafa, Desi, Dani, Yuyu, Nano (la mejor morcilla es la de León, y lo sabes), Alberto, Alejandrito y demás integrantes del grupo "Comeeeeer" por esos ratitos tan necesarios a la hora de la comida, desayuno o en cualquier otra franja horaria que se tercie. A los "mayores" Carol, Celia, Sergio y César porque sois un referente para los que empezamos y por ese buen rollo que desprendéis (Sergio, no me mates por lo de mayores :P).

I would like to acknowledge my co-authors Devaraj, Tanya and Sasha for their work and advises during this journey. I learned a lot from you. Also I want to thank the team from the drop tower, we spent nice moments in the lab. Gracias a Alvaro y José , por acogerme como una más cuando llegué a Enschede, por los cafés gratis de la máquina y las cervezas fuera de la uni. Peter, thank you for coming with me to Kangoo Jumps!

Yoli, gracias por seguir ahí aunque me haya vuelto una loca de las burbujas, por ser una gran amiga y compi de piso, y por tantos momentos vividos (festivales, tres mudanzas, dramas, viajes,...) y los que seguiremos viviendo juntas. A mis otros compis de piso y amigos durante estos años, Adri, María, Izar y Ana, porque llegar a casa después de que no funcione nada en el lab, preparar una cena rica o unas cervezas o ver una serie y echarnos esas risas que hacen que se te olvide todo lo malo del día no tiene precio. A Arantxa por tus audios mañaneros y conocimientos sobre la burbuja en la industria alimenticia, eres una grande.

A mi hermano Sergio y mi prima Vero (o debería decir la hermana del medio), porque ninguno de los tres se hubiera imaginado que yo acabaría haciendo un doctorado, y mira. Porque nos odiamos y nos queremos a partes iguales, y pase lo que pase siempre estáis ahí con vermut incluido. "Patri, dedícate

a la ciencia" (Sergio Vega, 2015) Sergio ¿recuerdas? A toda mi familia, no os nombro a todos que sois muchos, por preocuparos por mí y estar ahí. A mis padres, Elena y Carlos, por apoyarme tanto en mis errores (que son muchos) como en mis aciertos (que no son tantos), para mí sois los mejores. En definitiva a toda esa gente que durante este tiempo me ha hecho pensar desde diferentes perspectivas.